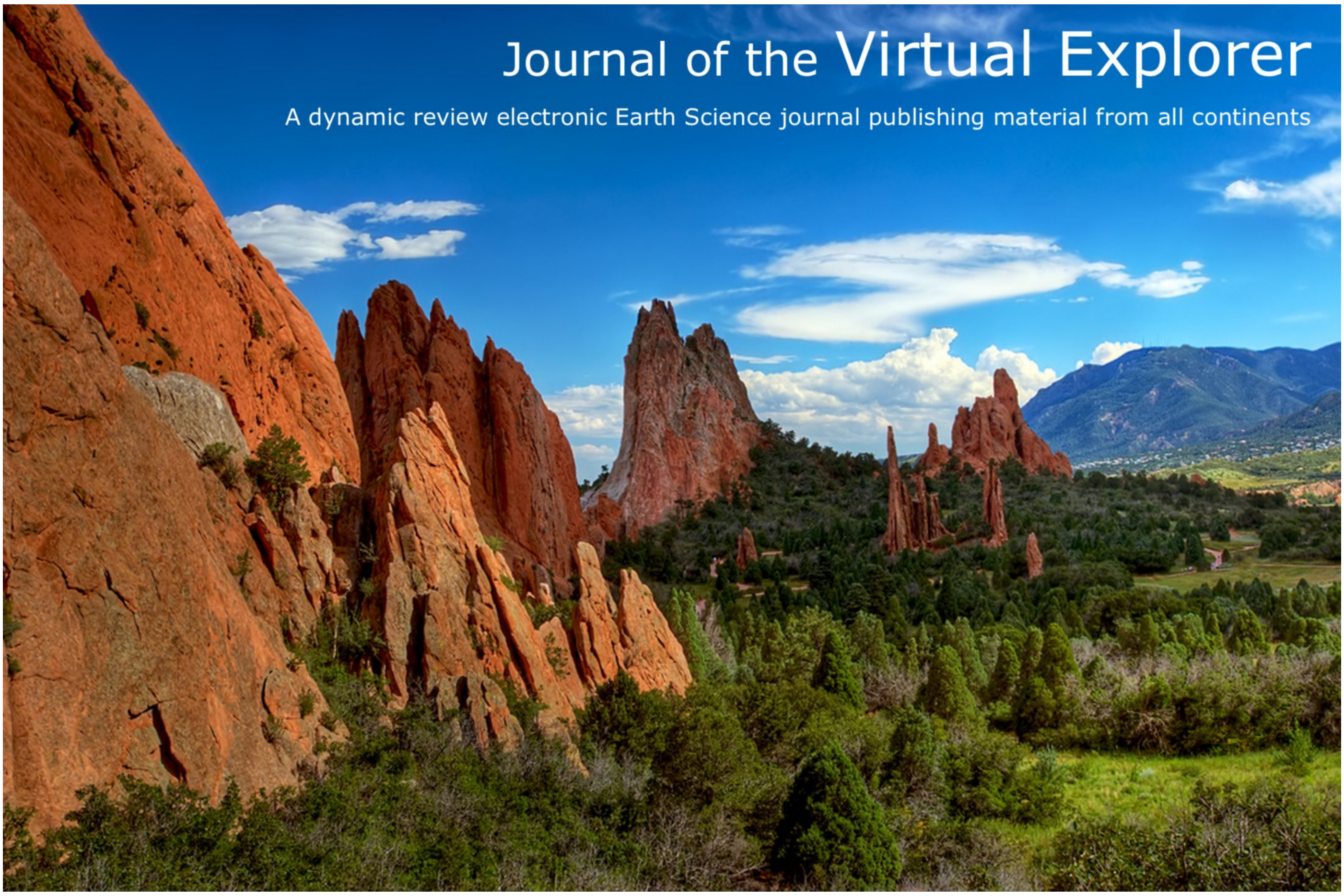

Structural and metamorphic features of the Main Central Thrust Zone and its contiguous domains in the eastern Nepalese Himalaya

Pietro Mosca, Chiara Groppo, Franco Rolfo

Journal of the Virtual Explorer, Electronic Edition, ISSN 1441-8142, volume **41**, paper 2
In: (Eds.) Michele Zucali, Maria Iole Spalla, and Guido Gosso,
Multiscale structures and tectonic trajectories in active margins, 2012.

Structural and metamorphic features of the Main Central Thrust Zone and its contiguous domains in the eastern Nepalese Himalaya

Pietro Mosca

CNR – Istituto di Geoscienze e Georisorse, Unità di Torino, Via Valperga Caluso 35, I-10125, Torino, Italy.
Email: p.mosca@csg.to.cnr.it

Chiara Groppo

Dipartimento di Scienze della Terra, Università di Torino, Via Valperga Caluso 35, I-10125, Torino, Italy.

Franco Rolfo

1. CNR – Istituto di Geoscienze e Georisorse, Unità di Torino, Via Valperga Caluso 35, I-10125, Torino, Italy.
2. Dipartimento di Scienze della Terra, Università di Torino, Via Valperga Caluso 35, I-10125, Torino, Italy.

Abstract: In the Kanchenjunga area (far eastern Nepal), as well as in the whole Himalayan chain, the juxtaposition of the high-grade mid-crustal Higher Himalayan Crystallines (HHC) onto the low grade Lesser Himalayan Sequence (LHS) is structurally marked by the Main Central Thrust Zone (MCTZ). On the base of original field mapping and meso- and micro-structural data, the MCTZ has been here identified as a crustal-scale ductile to ductile-brittle shear zone roughly centred on the Inverted Metamorphic Sequence (IMS), in which different rocks are more pervasively deformed and sheared with respect to adjacent rocks. The boundaries of the MCTZ are not represented by single thrusts. The lower boundary is marked by phyllonites and mylonitic schists located at the uppermost portions of the LHS at the contact with strongly mylonitic augen gneisses of the IMS. The upper boundary of the MCTZ is roughly located at the base of Grt-Kfs-Ky-Sil anatectic gneisses in the lower portion of the HHC, being itself characterized by pervasive ductile shearing.

Structural field data combined with petrologic results clearly indicate that the MCTZ is internally imbricated, resulting in the juxtaposition of rock packages characterized by different P-T evolutions and T/depth gradients, separated by “metamorphic discontinuities” which do not always correspond to evident structural breaks. This is the case of the metamorphic discontinuity identified at the upper structural levels of the IMS and juxtaposing the upper IMS rocks, locally anatectic, characterized by higher T/depth gradients on the lower IMS rocks, characterized by lower T/depth gradients. A similar metamorphic discontinuity was previously reported westward (Milke Danda transect) thus suggesting that it could be of regional importance in the tectonometmaoprhic architecture of eastern Nepal Himalaya.

Citation: 2012. Structural and metamorphic features of the Main Central Thrust Zone and its contiguous domains in the eastern Nepalese Himalaya . In: (Eds.) Michele Zucali, Maria Iole Spalla, and Guido Gosso, *Journal of the Virtual Explorer*, volume **41**, paper 2, doi: 10.3809/jvirtex.2011.00294

Introduction

The Main Central Thrust zone (MCTZ), one of the largest ductile shear zones currently known from any collisional orogen, is certainly one of the most debated tectonic features of the Himalaya (e.g. Searle *et al.*, 2008; Goscombe *et al.*, 2006 and references therein). The MCTZ is a north-dipping crustal-scale thrust zone, east-west striking for more than 2000 km throughout the whole Himalayan chain and characterized by a thickness ranging from ~100 m to several km. This major structure controlled the south-verging juxtaposition of the high-grade metamorphic rocks of the Higher Himalayan Crystallines (HHC) over the low-grade to non-metamorphic rocks of the Lesser Himalayan Sequence (LHS) (Fig. 1; Heim and Gansser 1939) and accommodated, upon the early Eocene, more than 100 km of crustal shortening (e.g. Schelling and Arita, 1991; Hodges, 2000) in the regional tectonic framework of the Asian and Indian plates collision (e.g. Le Fort, 1975).

Since the first detection and field mapping of this structure (Heim and Gansser 1939), a very rich literature illustrated its geological features across the whole Himalayan chain. Moreover, because of its significant lateral extension and consequent local variations, and because of a variable exposure due to vegetation and Quaternary cover, the precise identification and interpretation of the MCTZ are still object of debate, as well as the interpretation and origin of its associated (and largely documented) inverted metamorphism (e.g. Le Fort, 1975; Arita, 1983; Pêcher,1989; Searle and Rex, 1989; England and Molnar, 1993; Guillot, 1999; Harrison *et al.* 1999; Stephenson *et al.*, 2000; 2001; Goscombe *et al.*, 2006; Searle *et al.*, 2008; Groppo *et al.*, 2009 and references therein). Notably, in the Main Central Thrust Zone and its contiguous domains, the metamorphic grade increases from the lower to the upper structural levels, passing from the Bt-Chl zone in the LHS to the Sil-Kfs zone with extensive anatexis in the HHC.

Most of the published studies about the MCTZ are addressed to better define: i) its structural features (i.e. if it consists of one or more thrust faults, structural boundaries, ductile vs. brittle evolution), and ii) an accurate quantitative estimate of the metamorphic evolution and its relationship with the structural history. These are in fact key points for the development of any tectonic model aimed to the interpretation of the evolution of the Himalayan belt (e.g. Harrison *et al.*, 1999; Beaumont *et al.*, 2001, 2004; Grujic *et al.*, 2002 and references therein).

This paper deals with the Kanchenjunga area, located in the far-eastern Nepalese Himalaya, where the LHS outcrops as an tectonic half-window beneath the HHC (Fig. 1). This area is poorly known with respect to other sectors of the Himalayan chain, so far having been investigated in some detail by very few groups (Schelling and Arita, 1991; Schelling, 1992; Goscombe and Hand, 2000; Goscombe *et al.*, 2006; Imayama *et al.*, 2010). In 2009, an extensive field mapping, combined with structural and petrografic investigations, was done along the Tamor-Ghunsa Khola and the Simbuwa-Kabely Khola transects, crossing the Mirgin La to join them (Fig. 2). The main data of this fieldwork have been preliminarily illustrated and qualitatively discussed in a recent paper (Mosca *et al.*, 2011), mainly focused on the description of the most relevant meso- and micro- structural features of the area. The purpose of this novel contribution is to present new and more detailed quantitative data from the MCTZ and its contiguous domains, emphasizing the relationship between its structural evolution and metamorphic P-T conditions. Field investigations, meso- and micro-structural data were thus integrated with mineral chemistry data acquired on the most representative samples and with thermobarometric calculations. Moreover, the obtained results are compared with those previously obtained westward by our research group (Milke Danda transect: Groppo *et al.*, 2009) at similar structural levels, and discussed in the framework of the tectono-metamorphic architecture of this sector of the Himalayan chain.

Figure 1. Map and schematic of the study area

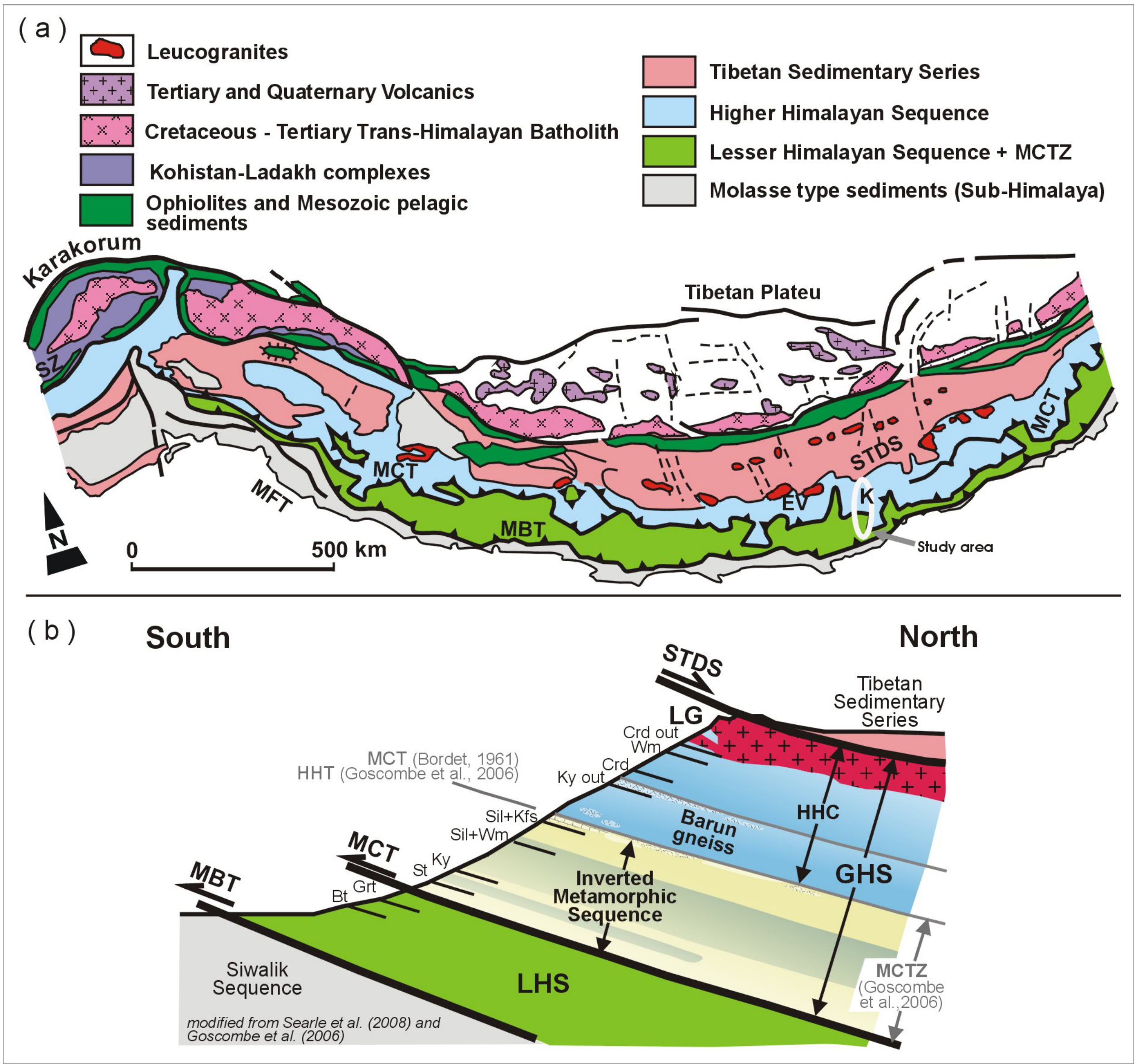

(a) Simplified tectonic sketch map of the Himalaya (redrawn after Dietrich and Gansser, 1981). The investigated area is outlined by the white ellipse. (b) Schematic cross-section across the Eastern Himalaya (modified from Goscombe *et al.*, 2006 and Searle *et al.*, 2008). EV, Everest; HHT, High Himal Thrust; K, Kangchenjunga; LG, leucogranites; LHS, Lesser Himalayan Sequence; MBT, Main Boundary Thrust; MCT, Main Central Thrust; MCTZ, Main Central Thrust Zone; MFT, Main Frontal Thrust; STDS, South Tibetan Detachment System; SZ, Indus/YarlungTsangpo Suture Zone. Mineral abbreviations for isograds are after Whitney and Evans (2010).

Figure 2. Geological map and representative cross-sections of the western Kangchenjunga region (modified from Mosca *et al.*, 2011).

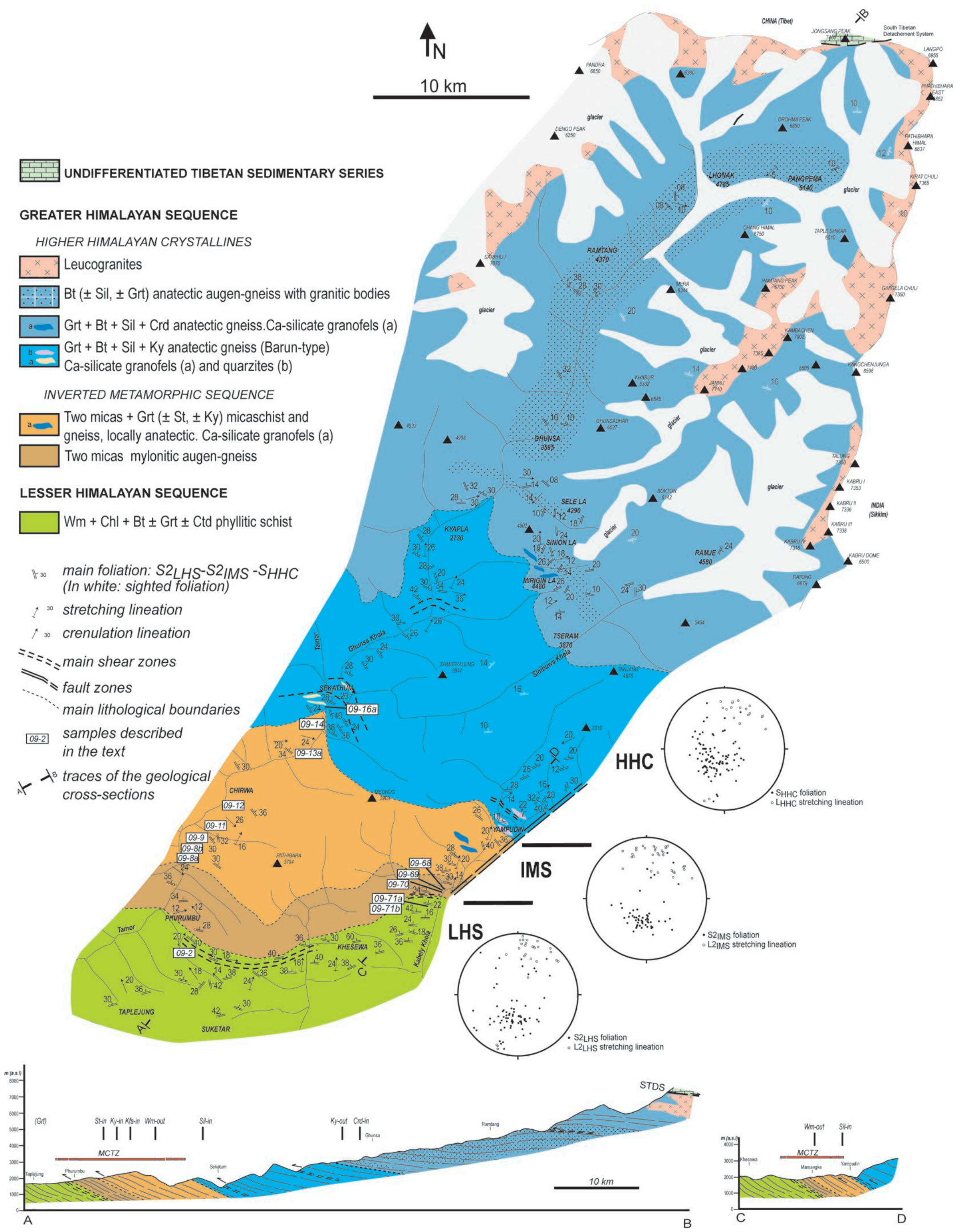

Stereoplots (Lower hemisphere equal-area projections) show the orientation of pervasive foliations and lineations in the LHS, IMS and HHC. See text for further explanations. Samples studied in this paper are reported in the map.

Regional tectonic setting

The Himalayan orogen is the result of the continent-continent collision between the Indian and Eurasian plates that began approximately around 55-50 million years ago and still continues today (e.g. Le Fort, 1996; Rowley, 1996; Guillot *et al.*, 2003; Leech *et al.*, 2005). Four main longitudinal tectonostratigraphic domains are usually distinguished along strike, bounded by north-dipping major tectonic discontinuities. From south to north, and from lower to upper structural levels, these are (Fig. 1) the Sub-Himalaya, the Lesser Himalayan Sequence (LHS), the Greater Himalayan Sequence (GHS) and the Tibetan Sedimentary Series (TSS).

The Sub-Himalaya domain consists of un-metamorphosed syn-orogenic sediments (sandstones, shales and conglomerates, also reported as “Siwalik group” in the literature) dated as Neogene and deposited on foreland basins. To the north, these deposits are bounded by the Main Boundary Thrust, along which they are thrusted by the LHS. The Lesser Himalayan Sequence consists mainly of low-grade metasediments (metapelitic schists and quarzites) associated with granitic orthogneiss (see for instance Upreti, 1999; Goscombe *et al.*, 2006; McQuarrie *et al.*, 2008, Khon *et al.*, 2010 and references therein). The LHS is subdivided into a number of stratigraphic and/or fault bounded units (e.g. Upreti, 1999; Paudel and Arita, 2000) and at a regional scale it forms a duplex structure (e.g. De Celles *et al.*, 1998; Mitra *et al.*, 2010). The LHS is bounded at its top to the north (Fig. 1) by the Main Central Thrust (MCT as originally defined by Gansser, 1964) that separates the LHS from the overlying GHS.

The Greater Himalayan Sequence, bounded to the north by the South Tibetan Detachment System (STDS; Burchfield *et al.*, 1992; Carosi *et al.*, 1998; Kellet *et al.*, 2010), consists from the lower to the upper structural levels of: (i) medium- to high grade metasediments and granitic orthogneisses roughly centred on the Inverted Metamorphic Sequence (IMS), its metamorphic grade increasing structurally upward from the staurolite zone to the sillimanite zone and, locally, to anatexis (e.g. Goscombe *et al.*, 2006; Groppo *et al.*, 2009, 2010). According to some authors the IMS is bounded at its top by a structural discontinuity (MCT of Bordet, 1961; High Himal Thrust – HHT - of Goscombe *et al.*, 2006, see Fig. 1 and the following discussion); (ii) high-grade para- and orto-gneisses, often anatectic, hosting networks and lens-shaped bodies of two-micas and tourmaline-bearing leucogranites, which can be as thick as 1-2 km at Mts. Makalu and Baruntse (Visonà and Lombardo, 2002) and up to 8 km thick at the Manaslu in Central Nepal (Guillot and LeFort, 1996). These high-grade gneisses are known as Higher Himalayan Crystallines (HHC) (Fig. 1) and are characterized by a progressive decrease in peak-pressure structurally upward (Pognante and Benna, 1993; Lombardo *et al.*, 1993; Davidson *et al.*, 1997; Guillot, 1999; Hodges, 2000; Groppo *et al.*, 2012).

The Tibetan Sedimentary Series overlie the HHC along the South Tibetan Detachment System and consist of Upper Precambrian to Eocene sediments originally deposited onto the Indian continental margin (Gaetani and Garzanti, 1991).

Geological and structural setting of the Kanchenjunga area

As concerning previous geologic studies in far east Nepal, the regional antiformal shape of the LHS beneath the GHS in the Kanchenjunga area could be already envisaged in the large-scale map drawn by Shresta *et al.* (1984). In the 1990’s, Schelling and Arita (1991) and Schelling (1992) significantly improved the tectonostratigraphy of the area: in particular, these authors placed the MCT between peculiar augen-gneiss (reported as the Sisne Khola Augen Gneiss) located at the upper structural levels of the LHS, and strongly-foliated garnet-biotite schists and gneisses (reported as the Junbesi Paragneiss) located at the base of the GHS. Furthermore, Schelling (1992) suggested that the MCTZ accommodated about 150 km of crustal shortening during thrusting of the GHS over the LHS.

More recently, Goscombe and Hand (2000) and Goscombe *et al.* (2006) placed the MCT at the base of the augen gneiss and envisaged at higher structural levels, within the GHS, the High Himal Thrust, a major structure controlling the metamorphic and deformational architecture of the orogen. The most recent paper about the Kanchenjunga area is a petrologic study of Imayama *et al.* (2010), which provides a metamorphic P-T profile across the western portion of the area described in this paper.

As concerning our contribution to clarifying the geologic setting of far east Nepal, a new geologic map of the western flank of the Kangchenjunga massif, based on field investigations and structural-petrographic studies and preliminary presented by Mosca *et al.* (2011) is reported in Fig. 2. In the map, the lithologies exposed in the Kanchenjunga area are ascribed to two tectonostratigraphic domains, showing at a regional scale both compositional layering and composite foliations dipping mainly to the N-NE and to the W. These are the LHS and the GHS, the latter being subdivided into the structurally lower Inverted Metamorphic Sequence (IMS) and in the structurally upper Higher Himalayan Crystallines (HHC). In particular, the IMS (described in detail below) identifies an heterogeneous and strongly mylonitic group of lithologies characterized by an increase in metamorphic grade towards upper structural levels and resting between typical schists of the LHS at its bottom and peculiar Grt + Kfs + Ky + Sil anatectic paragneiss of the HHC at its top (i.e. Barun Gneiss; Groppo *et al.*, 2012).

In the following, the mapped lithologies ascribed to the LHS, IMS and HHC are described from the lower to the upper structural levels (Fig. 2); Figs. 3 to 5 deal in particular with their main representative mesostructures. Microstructures of these rocks are shown by Figs. 6 to 9 in the next section, where petrography and mineral chemistry of the samples used in the “Average P-T” calculations will be detailed and discussed exhaustively.

Lesser Himalayan Sequence (LHS)

The LHS mainly consists of grey to pale-green fine-grained quartz-sericite schists, slates and phyllites (Fig. 3a), showing m-scale intercalations of either massive quartzites (±Grt ±Ctd) or chlorite-sericite schists. Cm-scale intercalations of garnet-amphibole quartzites are also observed, usually in the uppermost structural levels of the LHS, while graphite-rich schists occur locally towards the lower structural levels.

Figure 3. Representative mesostructures of the LHS

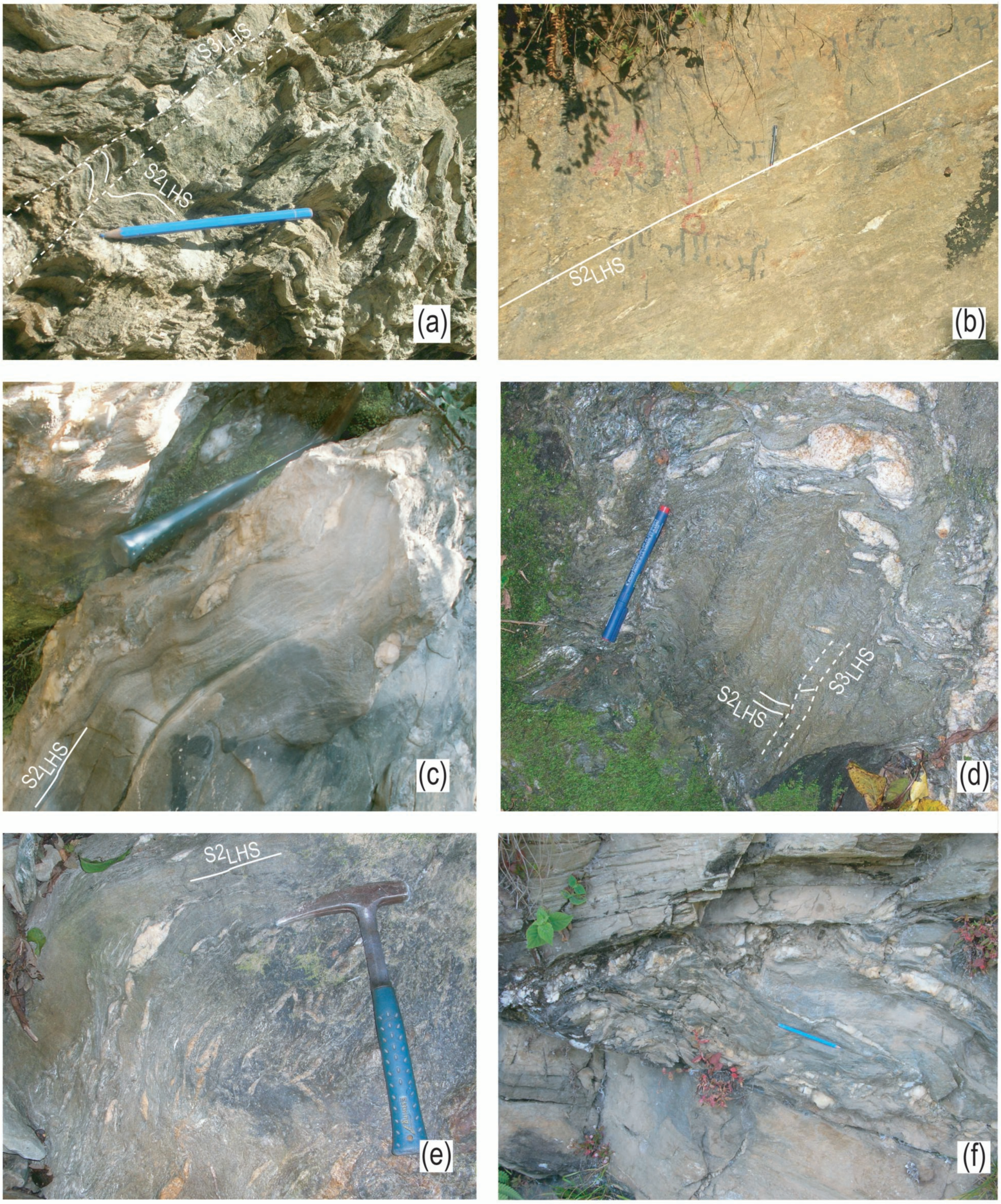

(a) Pale-green fine-grained slates showing relationships between $S2_{LHS}$ foliation and later $S3_{LHS}$ cleavage. (b) Quartz ribbons stretched along the main $S2_{LHS}$ foliation in the uppermost structural levels of the LHS. (c), (d) and (e) Decimetric to metric thick shear zones in the uppermost structural levels of the LHS, characterized by high concentration of quart in form of ribbons and/or boudins and deformed by a later folding event. (f) Detail of south-directed thrusting within the LHS.

The LHS shows widespread occurrence of a transpositive foliation, here labelled $S2_{LHS}$, defined by Qtz + Wm ± Chl ± Bt ± Grt (Figs. 3 and 6), and representing usually the most pervasive foliation recognizable and traceable at the outcrop-scale (see Fig. 2).

An older $S1_{LHS}$ foliation, usually preserved in microlithons, is defined by Qtz + Wm ± Chl and results parallel to lithological banding;

The $S2_{LHS}$ foliation corresponds to the axial plane foliation of asymmetrical tight south-verging $F2_{LHS}$ folds deforming the older $S1_{LHS}$ (and the lithological banding). Phyllosilicates defining the $S2_{LHS}$ occur in different proportions; usually muscovite is more abundant in the micaceous levels, whereas biotite and/or chlorite prevail in the quartz-rich domains. A $L2_{LHS}$ stretching lineation is widespread on the $S2_{LHS}$ surface, and is defined by aligned Wm, Bt and Qtz. $L2_{LHS}$ plunges to the N, thus resulting always almost parallel to the $S2_{LHS}$ dip (Fig. 2).

The $S2_{LHS}$ surface results more pervasively developed in the uppermost structural levels of the LHS, where the older planar fabrics are intensively transposed: outcrops show widespread occurrence of tight intrafolial folds and isolated fold hinges, and the lithological/$S1_{LHS}$ surfaces merge in the composite $S2_{LHS}$ surface. Approximately 500-800 m beneath the contact with the mylonitic augen-gneisses at the base of the IMS (as defined below), the LHS schists becomes thinly foliated (with phyllonitic appearance) due to a very pervasive mylonitic $S2_{LHS}$ foliation (Fig. 3b, d, e): in this portions, the older $S1_{LHS}$ is usually preserved in microlithons and locally occurs as spiral-shaped inclusion trails of quartz in garnet porphyroblasts (see in the following Figs. 6a, b, e, f).

At the outcrop scale, a partitioning of deformation within the LHS is indicated by dm to m thick shear zones, parallel to the mylonitic $S2_{LHS}$ foliation and locally characterized by high concentration of quartz in form of ribbons and/or boudins (Figs 3c, d, e). In these levels, quartz veins are stretched and rotated due to complex folding of the foliation, with axial planes both at high and low angles to shear planes (roughly corresponding to the $S2_{LHS}$ mylonitic foliation). Mica fish, S-C fabrics and internal thrusting (Fig. 3f) show consistent top-to-south shear movements.

Late asymmetric $F3_{LHS}$ folds and crenulations (Fig. 3a, d) with hinges trending from W-E to NW-SE, roughly orthogonal to the $L2_{LHS}$, show south-vergence. The axial planar foliation of these folds ($S3_{LHS}$) is only locally well developed and mainly defined by Wm ± Bt (Fig. 6d). More often, Wm + Bt ± Chl ± Ctd lepidoblasts statically overgrow the $S2_{LHS}$, without a clear $S3_{LHS}$ development (Fig. 6c, f).

Later deformations include open to chevron folds and crenulations, characterized by N-S to NNE-SSW trending hinges and exhibiting usually sub-vertical axial planes.

Greater Himalayan Sequence

Inverted Metamorphic Sequence

Schist and phyllonites of the LHS are overlied by a peculiar package of two mica augen-gneisses (Fig. 4a), well recognizable in the field with thickness on the order of 1500-2000 m along the Tamor-Ghunsa Khola and <1500 m along the Simbuwa-Kabely Khola. Within this lithology, m thick intercalations of chloritic schists and small mafic enclaves elongated parallel to the main foliation are locally observed (Fig. 4b). On the basis of their petrography and structural position, these augen-gneisses (Sisne Khola Augen Gneiss of Schelling, 1992) have been correlated to the Ulleri Gneiss of central Nepal (e.g. Le Fort, 1975; Arita, 1983). Upwards, the augen-gneisses pass to a few km thick package of two micas + garnet (± St ± Ky ± Kfs) schists (Fig. 4c) and gneisses, locally anatectic (Fig. 4d) toward upper structural levels, hosting m thick bodies of calc-silicate granofels and quarzites interbedded within the main foliation.

Figure 4. Representative mesostructures of the IMS

(a) Typical appearance of the two micas mylonitic augen gneiss: the large K-feldspar porphyroclasts are enveloped by the main $S2_{IMS}$ foliation defined by muscovite and biotite. (b) $S_m$all mafic enclave elongated parallel to the main $S2_{IMS}$ mylonitic foliation. (c) Transposition of lithological boundaries by $S2_{IMS}$ mylonitic foliation. (d) anatectic gneiss in the upper structural levels of the IMS. (e) Detail of mylonite derived from augen-gneiss, showing quartz ribbons stretched along the main $S2_{IMS}$ mylonitic foliation. (f) Strongly foliated augen-gneiss with top-to-the-south sense of shear obtained from rotation of K-feldspar porfiroclasts. a, c and f modified from Mosca *et al.*, 2011.

All the lithologies included in the IMS are highly deformed and have a strong mylonitic fabric (Fig. 4), thus making often difficult to identify and correlate the different planar fabrics among different outcrops. Moreover, at the upper structural levels of the IMS, partial melting locally affects some lithologies. In the anatectic rocks, the development of oriented structures is not only controlled by deformational events, but also by the production, extraction and crystallization of the melt (e.g. Solar, 2008); therefore the correlation between the main foliation recognised in the lower IMS and that recognised in the upper IMS is not trivial. For this reason, the neutral notation S_m (main schistosity) has been used locally for the anatectic samples (see in the following Fig. 9).

A dominant mylonitic foliation defined by Wm + Bt ± Ky ± St, here labelled $S2_{IMS}$, characterizes the lower IMS (see also Fig. 7. This foliation causes the intense transposition and consequent parallelization of the original compositional layering (Fig. 4c) and of at least an older $S1_{IMS}$ metamorphic foliation (Fig. 9). The $S1_{IMS}$ is preserved in microlithons as well as in form of spiral-shaped inclusions trails of Qtz ± Ilm ± Rt in garnet porphyroblasts locally enveloped by the $S2_{IMS}$ (Fig. 9). The $S2_{IMS}$ foliation corresponds to the axial plane foliation of $F2_{IMS}$ isoclinal to asymmetric south-verging tight folds deforming $S1_{IMS}$/lithological banding. The $S2_{IMS}$ dips to the north (Fig. 2) and contains a pervasive stretching lineation defined by elongated K-feldspar porphyroclasts in the augen-gneisses, and by the preferred alignment of minerals or mineral aggregates (Bt, Wm, St and Ky) in the schists. The orientation of the stretching lineation is always parallel or slightly oblique to the dip-direction of the $S2_{IMS}$ foliation (Fig. 2). Kinematic indicators such as rotated K-feldspar porphyroclasts showing both sigma-type and delta-type geometries, mica-fish and common S-C fabrics, uniformly define a consistent top-to-south sense of shear.

The $S2_{IMS}$ foliation is in turn deformed by later south-verging ENE-WSW trending folds and crenulation, thus suggesting a protracting history of the south-verging shearing in post-$S2_{IMS}$ time; this deformation is associated to a reactivation of the $S2_{IMS}$ foliation along the limbs of the asymmetric folds, evolving then in slip surfaces.

At the base of the IMS, meso- and microstructural observations suggest that the whole package of augen-gneisses was a site of high strain concentration. Augen-gneisses generally show a strongly mylonitic texture with large (often > 3 cm) K-feldspar porphyroclasts enveloped by the pervasive $S2_{IMS}$ mylonitic foliation defined by Wm + Bt. Quartz often occurs in mm to cm thick elongated ribbons and stretched bodies, parallel to the mylonitic foliation (Fig. 4e). Rare outcrops show less deformed portions, roughly preserved as macro-lithons. Within strongly foliated augen-gneisses (Fig. 4f), K-feldspar occurs as porphyroclasts widely dispersed through a fine-grained foliated matrix of feldspar, quartz and micas. In general, the presence of large K-feldspar porphyroclasts made the rock mechanically inhomogeneous, thus causing a local pronounced perturbation of the shear planes ($S2_{IMS}$ foliation) within the sheared rock bodies.

Higher Himalayan Crystallines

The HHC represent the upper part of the GHS, bounded by the STD at its top. At the lower structural levels, the HHC consist of peculiar Grt + Kfs + Sil ± Ky anatectic paragneiss (Fig. 5a), with local intercalations of quarzite, impure marble and calc-silicate rock with the assemblage Di + Pl + Qtz ± Grt ± Amp (Fig. 5b, c). These gneisses (Rolwaling-Khumbu-Kangchenjunga Paragneiss in Schelling, 1992 and Jannu-Kangchenjunga Gneiss in Goscombe *et al.*, 2006) are here considered to be the lateral equivalents of the Barun gneiss occurring in the Everest-Makalu region (Lombardo *et al.*, 1993; Groppo *et al.*, 2012).

Figure 5. Representative mesostructures of the HHC

(a) Grt + Kfs + Ky + Sil anatectic paragneiss ("Barun type"). S_{HHC} foliation is defined by a peculiar compositional layering. (b) and (c) examples of boudins of calc-silicate granofels consisting of Pl + Grt + Di + Qtz within the "Barun type" paragneiss, stretched and enveloped by the main S_{HHC} foliation. (d) Anatectic orthogneiss, with development of a ductile shear zone roughly parallel to the main S_{HHC} foliation, in turn crosscut by a pegmatite dike. (e) Pegmatitic and aplitic dikes variably oriented with respect to the main S_{HHC} foliation in the cordierite-bearing paragneiss. (f) Ductile shear zone developed in the upper levels of the HHC. a and c modified from Mosca *et al.*, 2011.

The upper structural levels of the HHC consist of Bt + Sil + Crd ± Grt anatectic paragneisses, lacking kyanite and characterized by the occurrence of cordierite in significant amounts, and associated to large bodies of sillimanite-bearing anatectic orthogneisses (Fig. 5d). Pegmatitic dykes and leucogranite significantly increase towards higher structural levels (Fig. 2), variably oriented with respect to the main foliation (Fig. 5d, e).

It is generally difficult to give an univocal interpretation of all the penetrative structures and fabrics recognizable in the field in the high-grade lithologies of the HHC (Fig. 5), namely if they result from tectonic or from migmatization and/or melt-crystallization processes. At the outcrop scale, the HHC show a pervasive foliation usually parallel to the mesoscopic compositional layering and dipping at moderate angle towards the north and the east; this foliation has been generally reported and mapped as S_{HHC} in the Fig. 2.

In the lower structural levels of the HHC (Fig. 5a), the S_{HHC} foliation of the Barun-type gneiss is defined by millimetric to centimetric leucocratic domains rich in quartz and feldspar alternating with millimetric dark Bt + Pl + Sil layers. Garnet is always present and occurs as mm to cm large porphyroblasts generally enveloped by the Bt + Pl + Sil foliation, or within the leucocratic domains. A stretching mineral lineation L_{HHC}, defined by aligned Sil, Qtz and Bt, is recognizable on the S_{HHC} and plunges parallel to the S_{HHC} dip. Dm to several m thick bodies of calc-silicate granofels (Fig. 5b, c), quarzites and marbles are observed stretched along very pervasive S_{HHC} planes, often concentrated at the contact with the IMS schists and gneiss.

Moving structurally upwards, the S_{HHC} identifies a pervasive foliation both in the Bt + Sil + Crd ± Grt anatectic paragneisses and in the Sil-bearing anatectic orthogneisses, respectively defined by Qtz + Feld + Bt + Sil + Cr, and Qtz + Feld + Bt + Sil assemblages. In the Sil-bearing anatectic orthogneisses, cm-scale K-feldspar porphyroclasts are stretched and rotated along the S_{HHC} (Fig. 5d), and widespread S-C fabrics and rotational K-feldspar porphyroclasts define a top-to-south sense of shear.

Throughout the HHC, the S_{HHC} is variably folded, displaced and deformed with irregular sigmoidal patterns in correspondence of, and within, ductile shear zones, ranging from a few cm up to a few m in thickness (Fig 5f). Most of these zones are at low to moderate angles with respect to the pervasive S_{HHC}. Peculiar late shear zones, characterized by significant grain reduction and penetrative low-grade metamorphic foliation, have been identified in few outcrops at the lowermost structural levels (Mosca *et al.*, 2011).

Field observation along the two studied transects suggest a significant increase of the mesoscale-folding of S_{HHC} passing from the lower structural levels (Barun-type gneiss) towards the higher structural levels. In particular, the Crd-bearing anatectic gneiss is often deformed by folds exhibiting isoclinal geometry with thickened hinges and thinned limbs, and axial planes sub-horizontal or dipping toward the NW.

The Main Central Thrust zone in the Kanchenjunga area

According to a large number of field studies and interpretations from several sectors of the Himalaya, structural criteria are primary references to define and identify the MCTZ (see for instance Searle *et al.*, 2009 and references therein for an exhaustive critical review).

Structural mapping in the Kanchenjunga area shows that, at the juxtaposition of the HHC over the LHS, the MCTZ identifies a ductile to ductile-brittle shear zone roughly centred on the IMS and showing minimum thickness on the order of 6-7 km in the north-western portion and 3-4 km in the south-eastern portion of the studied region (see transects of Fig. 2; Mosca *et al.* 2011). The boundaries of the MCTZ in the investigated areas cannot be traced along a single thrust or a set of adjacent discrete thrusts, but are recognized as zones of high strain, affecting both the upper portions of the LHS and the lower portions of the HHC (see also Mosca *et al.*, 2011) where an increasing of the intensity of the shear is observed at the outcrop scale.

Following this rationale, the lower boundary of the MCTZ is progressively marked by the common occurrence of phyllonites and mylonitic schists in the uppermost portions of the LHS near to the contact with the strongly mylonitic augen-gneisses of the lower IMS. The upper boundary of the MCTZ is marked in the lower portion of the Barun-type gneiss by evidence of pervasive ductile shearing and boudinage. Throughout the whole MCTZ, a widespread pervasive development of mylonitic foliations is observed, parallel (at the map scale) to the main lithological contacts, as well as abundant kinematic indicators showing a consistent top to the south sense of shear.

Petrography and mineral chemistry

Herein, the micro-structural features and mineral compositions of three selected samples from the LHS and nine selected samples from the IMS are described in detail, with the aim of correlating their structural and metamorphic evolutions. Relevant microstructures are illustrated in Figs. 6 to 9.

The rock-forming minerals were analysed with a Cambridge Stereoscan 360 SEM equipped with an EDS Energy 200 and a Pentafet detector (Oxford Instruments) at the Department of Earth Sciences, University of Torino. The operating conditions were: 50 seconds counting time and 15 kV accelerating voltage. SEM-EDS quantitative data (spot size = 2μm) were acquired and processed using the Microanalysis Suite Issue 12, INCA Suite version 4.01; natural mineral standards were used to calibrate the raw data; the ΦρZ correction (Pouchou and Pichoir, 1988) was applied. Representative mineral chemistry data are reported in Tables 1-5 and plotted in diagrams of Fig. 10. Links to tables: Table 1, Table 2, Table 3, Table 4, Table 5.

A synthesis of the assemblages-deformation relations is reported in Fig. 11.

Lesser Himalayan Sequence

Sample 09-2

Microstructure

Sample 09-2 is a fine-grained two-micas + chlorite phyllite consisting of mm thick micaceous levels alternated with quartz-rich domains and locally overgrown by porphyroblastic garnet (Fig. 6a, c). In both domains, the main foliation ($S2_{LHS}$) is defined by the preferred orientation of white mica, biotite and chlorite, in different modal proportions: Wm >> Bt > Chl in the micaceous levels and Bt ≈ Chl >> Wm in the quartz-rich domains. The $S2_{LHS}$ results from the transposition of an older $S1_{LHS}$ foliation still preserved in the microlithons (Fig. 6a, b) and defined by chlorite, white mica and biotite (Chl > Wm > Bt). The $S2_{LHS}$ is locally overgrown by porphyroblastic pink garnet up to several mm in diameter, replaced at the rim and along fractures by a thick corona of chlorite + minor biotite (Fig. 6a). The internal schistosity preserved in garnet porphyroblasts is continuous with the $S2_{LHS}$ and is mainly defined by the alignment of fine-grained ilmenite, quartz and minor epidote. Beside garnet, abundant white mica and biotite lepidoblasts (Fig. 6b, c), hundreds of microns in length, and very rare plagioclase granoblasts and epidote statically overgrow the $S2_{LHS}$.

A later, mm spaced, planar foliation ($S3_{LHS}$) nearly orthogonal to the main foliation results from the crenulation of the $S2_{LHS}$; this $S3_{LHS}$ foliation is only locally evident and is defined by white mica + biotite, as well as by the alignment of ilmenite (Fig. 6d).

Mineral chemistry

The different phyllosilicate generations, clearly recognisable on microstructural basis, are less easily distinguishable on chemical basis being their compositions often overlapped (Fig. 10a, c). White mica shows a Si content in the range 3.06-3.19 a.p.f.u. (on the basis of 11 oxygens); its Na content is inversely proportional to Si and in the range 0.08-0.16 a.p.f.u. On average, white mica in the $S1_{LHS}$ and $S2_{LHS}$ foliations shows higher Si and lower Na contents (Si=3.08-3.19 a.p.f.u.; Na=0.08-0.13 a.p.f.u.) than white mica in the $S3_{LHS}$ and white mica statically overgrowing the $S2_{LHS}$ (Si=3.06-3.14 a.p.f.u.; Na=0.10-0.16 a.p.f.u.). Muscovite flakes statically overgrowing the $S2_{LHS}$ foliation are slightly zoned, with Si decreasing and Na increasing from core to rim. Biotite shows a Ti content in the range 0.10-0.15 a.p.f.u. (on the basis of 11 oxygens) and a slightly variable X_{Mg} (X_{Mg}=0.32-0.34), inversely proportional to Ti. Biotite in the $S1_{LHS}$, $S2_{LHS}$ and $S3_{LHS}$ are hardly distinguishable (Ti=0.12-0.15 a.p.f.u.; X_{Mg}=0.32-0.33), whereas biotite flakes statically overgrowing the $S2_{LHS}$ have a slightly lower Ti content (Ti=0.10-0.12 a.p.f.u.) counterbalanced by a higher X_{Mg} (X_{Mg}=0.33-0.34). All the chlorite generations have a Si content in the range 5.07-5.31 a.p.f.u. (on the basis of 36 oxygens) and a X_{Fe}=0.64-0.65: therefore, they can be classified as ripidolite according to Hey (1954).

Garnet porphyroblasts are strongly zoned (Fig. 10b): the bell-shaped X_{Mn} and X_{Ca} decrease from core to rim (X_{Mn} from 0.16 to 0.04; X_{Ca} from 0.16 to 0.13) is counterbalanced by an increase in both X_{Fe} and X_{Mg} (X_{Fe} from 0.65 to 0.77; X_{Mg} from 0.04 to 0.06). The few plagioclase granoblasts overgrowing the $S2_{LHS}$ are oligoclase (Fig. 10d), showing an anorthite content in the range 0.16-0.24, with the lower values toward the rim.

Figure 6. Representative microstructures of LHS samples

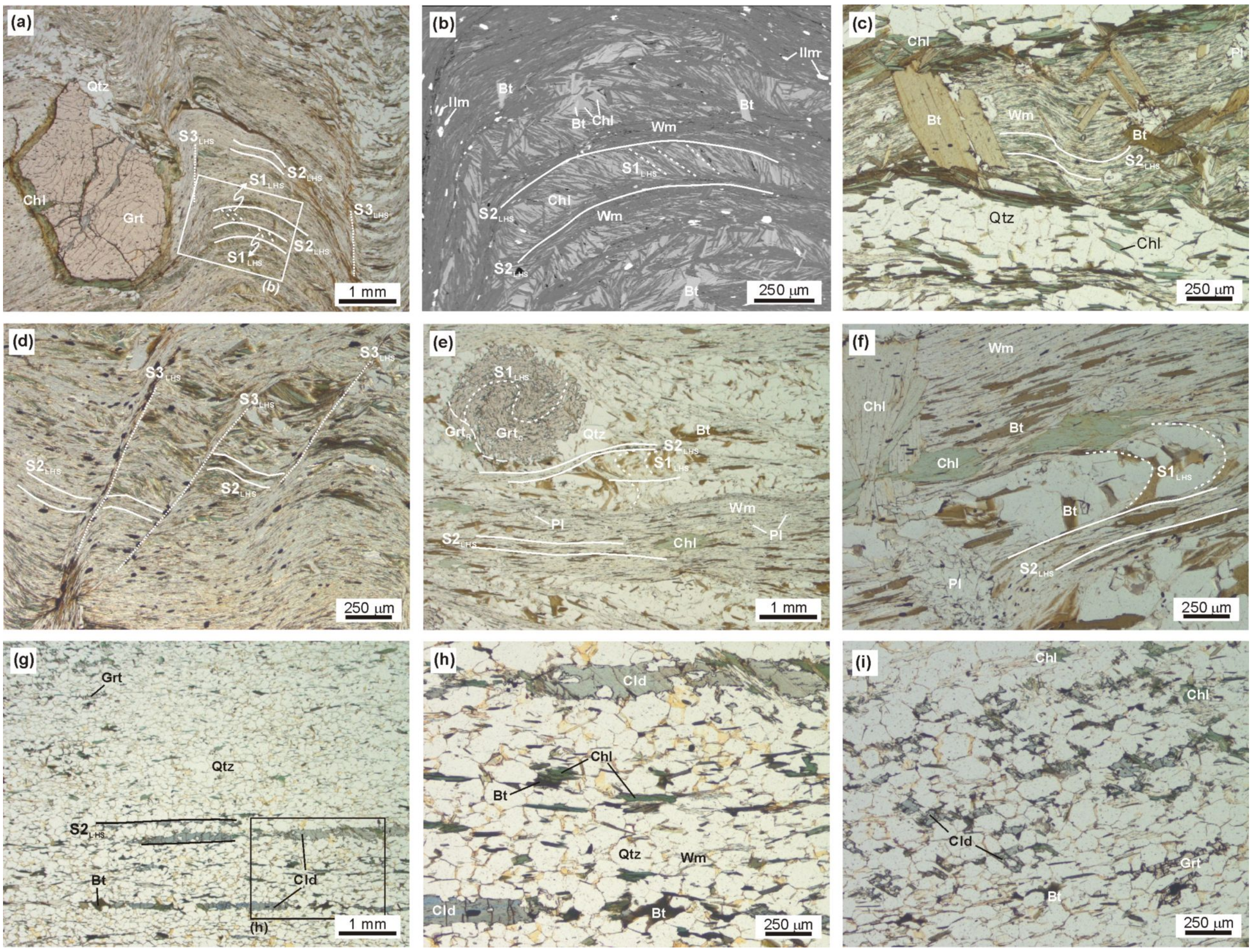

Sample 09-2. (a) Garnet porphyroblast overgrowing the main foliation $S2_{LHS}$ defined by muscovite, biotite and chlorite. The $S2_{LHS}$ is crenulated, with the local development of a later $S3_{LHS}$ foliation, defined by muscovite and biotite. Plane Polarized Light (PPL). (b) Detail of (a), showing microlithons preserving the evidence of an older $S1_{LHS}$, defined by chlorite, muscovite and biotite. Note the biotite flakes statically overgrowing the $S2_{LHS}$. Back Scattered Electron image (BSE). (c) Detail of a micaceous level alternated to a quartz-rich domain (note the different modal proportions of phyllosilicates in the two levels). In the micaceous layer, large biotite flakes statically overgrow the $S2_{LHS}$ foliation (PPL). (d) Detail of the $S3_{LHS}$ foliation derived from the crenulation of the main $S2_{LHS}$ foliation (PPL). Sample 09-71a. (e) Snowball garnet porphyroblast mostly enveloped by the main $S2_{LHS}$ foliation, except for its rim GrtR. Garnet core (GrtC) includes a rotated internal foliation ($S1_{LHS}$) defined by quartz. The $S1_{LHS}$ is also preserved in the microlithons, where it is defined by muscovite and biotite (PPL). (f) Detail of the $S2_{LHS}$ foliation, defined by muscovite and biotite and derived from the transposition of an older $S1_{LHS}$ foliation. Note chlorite and plagioclase porphyroblasts overgrowing the $S2_{LHS}$ (PPL). Sample 09-71b. (g) Microstructure of the chloritoid-bearing quartzite (PPL). (h) Detail of the $S2_{LHS}$ foliation, defined by the alignment of muscovite, biotite, chlorite and chloritoid. The same minerals also overgrow the main foliation (see the top of the microphoto) (PPL). (i) Detail of chloritoid and garnet scheletric crystals (PPL). a and b modified from Mosca *et al.*, 2011.

Sample 09-71a

Microstructure

Sample 09-71a is a phyllitic two-micas schist with snowball garnet porphyroblasts enveloped by a continuous planar foliation defined by mm thick mica-rich layers alternated with quartz-rich domains (Fig. 6e). The main foliation ($S2_{LHS}$), defined by the preferred orientation of white mica and biotite (Wm > Bt), transposes an older $S1_{LHS}$ foliation preserved in the microlithons (Fig. 6e, f) and defined by both white mica and biotite. The snowball garnet porphyroblasts, several mm in diameter, are mostly enveloped by the $S2_{LHS}$ and contain a rotated internal foliation mainly defined by quartz + minor ilmenite and epidote (Fig. 6e). However, the outermost garnet rims are almost free of inclusions and are in equilibrium with the $S2_{LHS}$, thus suggesting that garnet growth could have begun synchronously with the development of the $S1_{LHS}$ foliation but ceased at the beginning of the $S2_{LHS}$ development. Quartz, white mica and biotite occur in the pressure shadows of garnet, whereas chlorite and biotite locally replaces garnet at the outermost rim.

Large chlorite lepidoblasts (often in aggregates of radially oriented flakes), plagioclase porphyroblasts and minor biotite and white mica flakes statically overgrow the $S2_{LHS}$ (Fig. 6f).

Mineral chemistry

The three different white mica generations ($S1_{LHS}$, $S2_{LHS}$ and post-$S2_{LHS}$) show very similar chemical composition and therefore they are hardly distinguishable on chemical basis (Fig. 10c). Their Si content ranges between 3.07 and 3.16 a.p.f.u. and Na is in the range 0.11-0.21 a.p.f.u. Biotite compositions are more informative (Fig. 11a): biotite in the $S1_{LHS}$, in fact, shows on average a slightly lower Ti content and a slightly higher X_{Mg} (Ti=0.10-0.11 a.p.f.u.; X_{Mg}=0.38-0.39) than biotite in the $S2_{LHS}$ and biotite overgrowing the main foliation (Ti=0.10-0.12 a.p.f.u.; X_{Mg}=0.37-0.38). Chlorite is homogeneous in composition and it may be classified as a ripidolite (Si=5.15-5.35 a.p.f.u.; X_{Fe}=0.56-0.60).

Garnet is zoned and the transition from core to rim is quite sharp (Fig. 10b). Garnet core, corresponding to the snowball central portion of the porphyroblasts, shows a progressive but significant decrease of X_{Mn} and X_{Ca} (X_{Mn} from 0.22 to 0.01; X_{Ca} from 0.22 to 0.11) counterbalanced by an increase in X_{Fe} and X_{Mg} (X_{Fe} from 0.55 to 0.80; X_{Mg} from 0.02 to 0.08). On the opposite, garnet rim, corresponding to the outermost portion of the porphyroblasts almost free of inclusions, is homogeneous in composition (X_{Mn}=0.00; X_{Ca}=0.11; X_{Fe}=0.80; X_{Mg}=0.09). Plagioclase porphyroblasts overgrowing the $S2_{LHS}$ foliation are oligoclase (Fig. 11d), with anorthite content decreasing from core (X_{Ca}=0.23) to rim (X_{Ca}=0.18).

Sample 09-71b

Microstructure

Sample 09-71b is a chloritoid + garnet -bearing quartzite occurring as a m thick intercalation within the phyllitic two-micas schist 09-71a. The main discontinuous foliation $S2_{LHS}$ is defined by the preferred orientation of white mica, dark brown biotite and very dark green chlorite (Wm > Bt ≈ Chl) (Fig. 6g, h). Chloritoid mainly occurs as scheletric, bluish-green crystals elongated in sub-millimetric levels; also garnet (much more rare) is scheletric and elongated parallel to the $S2_{LHS}$ (Fig. 76i). Chloritoid, chlorite, biotite and white mica also occur in crystals discordant with respect to the main foliation (Fig. 6h, i), probably representing a post-$S2_{LHS}$ assemblage statically overgrowing the $S2_{LHS}$.

Mineral chemistry

Mineral compositions reflect a relatively Fe-rich bulk rock composition. The dark brown biotite defining the $S2_{LHS}$ foliation shows a Ti content in the range 0.07-0.11 a.p.f.u. and a very low X_{Mg} (X_{Mg}=0.09-0.13); biotite flakes overgrowing the $S2_{LHS}$ differ for the slightly higher Ti content (Ti=0.11-0.12 a.p.f.u.). White mica in the $S2_{LHS}$ foliation has Si=3.08-3.15 a.p.f.u. and Na=0.03-0.05 a.p.f.u., whereas white mica post-$S2_{LHS}$ shows a lower Si content, in the range 3.02-3.12 a.p.f.u. (Fig. 10c). The two chlorite generations do not show significant differences in composition and may be classified as ripidolite and daphnite (Si=5.00-5.12 a.p.f.u.; X_{Fe}=0.88-0.90).

Chloritoid elongated parallel to the $S2_{LHS}$ differs from chloritoid overgrowing the main foliation for its slightly lower X_{Mg} ($S2_{LHS}$: X_{Mg}=0.05-0.06; post-$S2_{LHS}$: X_{Mg}=0.06-0.08). Garnet is mainly an almandine (X_{Fe}=0.88-0.90), with very little amounts of pyrope, grossular and spessartine components (X_{Mg}=0.04-0.05; X_{Ca}=0.03; X_{Mn}=0.03-0.04) (Fig. 10b).

Inverted Metamorphic Sequence

Sample 09-68

Microstructure

Sample 09-68 is a two-micas augen-gneiss, with albitized K-feldspar porphyroclasts up to few cm in length enveloped by a mylonitic foliation ($S2_{IMS}$) (Fig. 7a). The $S2_{IMS}$ mylonitic foliation is defined by the preferred orientation of muscovite and biotite (Wm >> Bt), associated to fine-grained quartz and plagioclase and concentrated in millimetric layers alternated to coarse-grained quartzo-feldspathic domains (Fig. 7b). The large K-feldspar porphyroclasts are completely replaced by large albite crystals; rare interstitial grains of microcline have been observed in the quartzo-feldspathic domains (Fig. 7c). A later generation of muscovite and biotite flakes locally overgrows the $S2_{IMS}$ foliation (Fig. 7b). Tourmaline is present as accessory mineral: it is sharply zoned, with a dark green core and a green-yellow rim.

Figure 7. Representative microstructures of the IMS orthogneisses

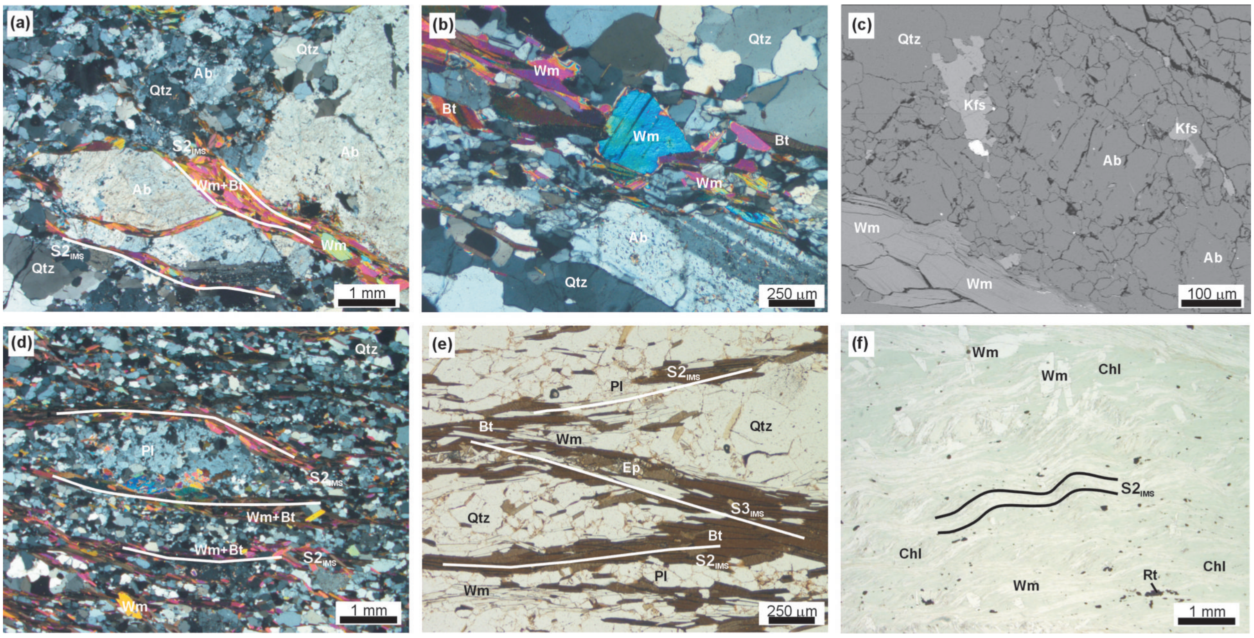

Sample 09-68. (a) Former K-feldspar porphyroclasts (now replaced by albite) enveloped by the main foliation $S2_{IMS}$, defined by muscovite and biotite. Note the quartz and albite grain reduction along the $S2_{IMS}$. Crossed Polarized Light (XPL). (b) Detail of the $S2_{IMS}$ foliation overgrown by a muscovite flake (XPL). (c) Detail of interstitial K-feldspar crystals within a fine-grained albite + quartz level (BSE). Sample 09-69. (d) $S2_{IMS}$ mylonitic foliation defined by muscovite and biotite and enveloping a plagioclase lenticular domain derived from the re-crystallization of former K-feldspar. Note the muscovite flakes overgrowing the main foliation (XPL). (e) Detail of a biotite + muscovite + epidote shear band ($S3_{IMS}$) crosscutting the $S2_{IMS}$ at low angles (PPL). Sample 09-70. (f) Detail of the muscovite + chlorite $S2_{IMS}$ mylonitic foliation crenulated and overgrown by large muscovite flakes (PPL).

Mineral chemistry

The two generations of white mica recognised on microstructural basis (i.e. defining the $S2_{IMS}$ foliation and statically overgrowing the $S2_{IMS}$) show a very similar composition (Fig. 10c), with a Si content in the range 3.16-3.24 a.p.f.u. and Na=0.04-0.05 a.p.f.u.. The Si content locally decreases down to 3.15 a.p.f.u. at the rim of post-$S2_{IMS}$ lamellae. Biotite defining the $S2_{IMS}$ foliation has Ti=0.11-0.17 a.p.f.u. and X_{Mg} in the range 0.41-0.46, inversely proportional to Ti. The post-$S2_{IMS}$ biotite differs for its slightly higher Ti content (Ti=0.17-0.19 a.p.f.u.) (Fig. 10a). Both plagioclase in the quartzo-feldspathic domains and plagioclase replacing K-feldspar porphyroclasts are almost pure albite (An_{1-3}) (Fig. 10d).

Sample 09-69

Microstructure

Sample 09-69 is a two-micas mylonitic orthogneiss with plagioclase-rich lenticular domains enveloped by the main foliation (Fig. 7d). The main, mm spaced, foliation ($S2_{IMS}$) is defined by the preferred orientation of biotite and muscovite (Bt > Wm) concentrated in sub-mm layers alternated with fine-grained quartzo-feldspathic domains. Very few relics of K-feldspar have been observed in the quartzo-feldspathic domains, although the fine-grained plagioclase-rich elongated domains enveloped by $S2_{IMS}$ foliation derive from the deformation and re-crystallization of former K-feldspar porphyroclasts). A discontinuous foliation ($S3_{IMS}$) defined by biotite and muscovite crosscuts at low angles the $S2_{IMS}$ foliation (Fig. 7e). S$_m$all epidote grains, locally with an allanitic core, overgrow the $S2_{IMS}$ and are associated to the Bt + Wm shear bands.

Mineral chemistry

No significant variations in the white mica composition have been observed as a function of its microstructural position (Fig. 10c). The Si content ranges between 3.11 and 3.20 a.p.f.u., and Na is in the range 0.03-0.05 a.p.f.u. Biotite shows a Ti content inversely proportional to X_{Mg}: biotite in the $S2_{IMS}$ foliation and statically overgrowing it has Ti=0.12-0.19 a.p.f.u. and X_{Mg}=0.33-0.39, whereas biotite in the later shear bands has a slightly higher Ti content and lower X_{Mg} (Ti=0.18-0.20 a.p.f.u.;

X_{Mg}=0.33-0.34) (Fig. 10a). Plagioclase is an oligoclase (An_{18-24}) (Fig. 10d), with the higher anorthite content corresponding to plagioclase granoblasts overgrowing the $S2_{IMS}$ foliation.

Sample 09-70

Microstructure

Sample 09-70 is a muscovite-chlorite schist occurring as a m thick intercalation within the mylonitic orthogneiss 09-69. The pervasive mylonitic foliation ($S2_{IMS}$) is defined by the preferred orientation of both white mica and pale-green Mg-rich chlorite, whilst an older foliation ($S1_{IMS}$) is still preserved in the microlithons and defined by the same assemblage. Abundant large muscovite flakes statically overgrow the $S2_{IMS}$ (Fig. 7f). Apatite and rutile are abundant as accessory phases.

Mineral chemistry

Muscovite and chlorite compositions are quite homogeneous in both the $S2_{IMS}$ and $S1_{IMS}$. The Si content of muscovite ranges between 3.03 and 3.10 a.p.f.u. (Na=0.17-0.31 a.p.f.u.), and X_{Fe} in chlorite is low (X_{Fe}=0.28-0.29).

Sample 09-8b

Microstructure

Sample 09-8b is a two-micas, garnet-bearing micaschist consisting of a regular alternation of cm thick muscovite-rich vs. biotite-rich levels, probably reflecting the original juxtaposition of pelitic vs. psammitic layers in the sedimentary protolith. Mineral assemblages and compositions in the two levels are different and will be described separately. The transition from the metapelitic to the metapsammitic level is gradual and occurs through a progressive decrease in the white mica and chlorite modal amounts counterbalanced by an increase in biotite content.

The metapelitic level mainly consists of quartz, muscovite, chlorite, garnet, biotite, staurolite, very minor kyanite and accessory ilmenite and allanite. The main foliation ($S2_{IMS}$) is defined by the preferred orientation of muscovite, chlorite and biotite (Wm >> Chl > Bt) and envelops very large garnet porphyroclasts up to 1 cm in diameter. Garnet porphyroclasts are microstructurally zoned: garnets core includes an internal foliation ($S1_{IMS}$) discordant with respect to the $S2_{IMS}$ and defined by quartz and ilmenite, whereas garnets rim is almost free of inclusions and seems in equilibrium with the $S2_{IMS}$ foliation (Fig. 8a). Staurolite occurs as small granoblasts either aligned with the $S2_{IMS}$ foliation or statically overgrowing it (Fig. 8a). Kyanite is very rare and overgrows the main foliation, partially replacing staurolite (Fig. 8d).

Figure 8. Representative microstructures of the IMS metapelitic samples (not-anatectic)

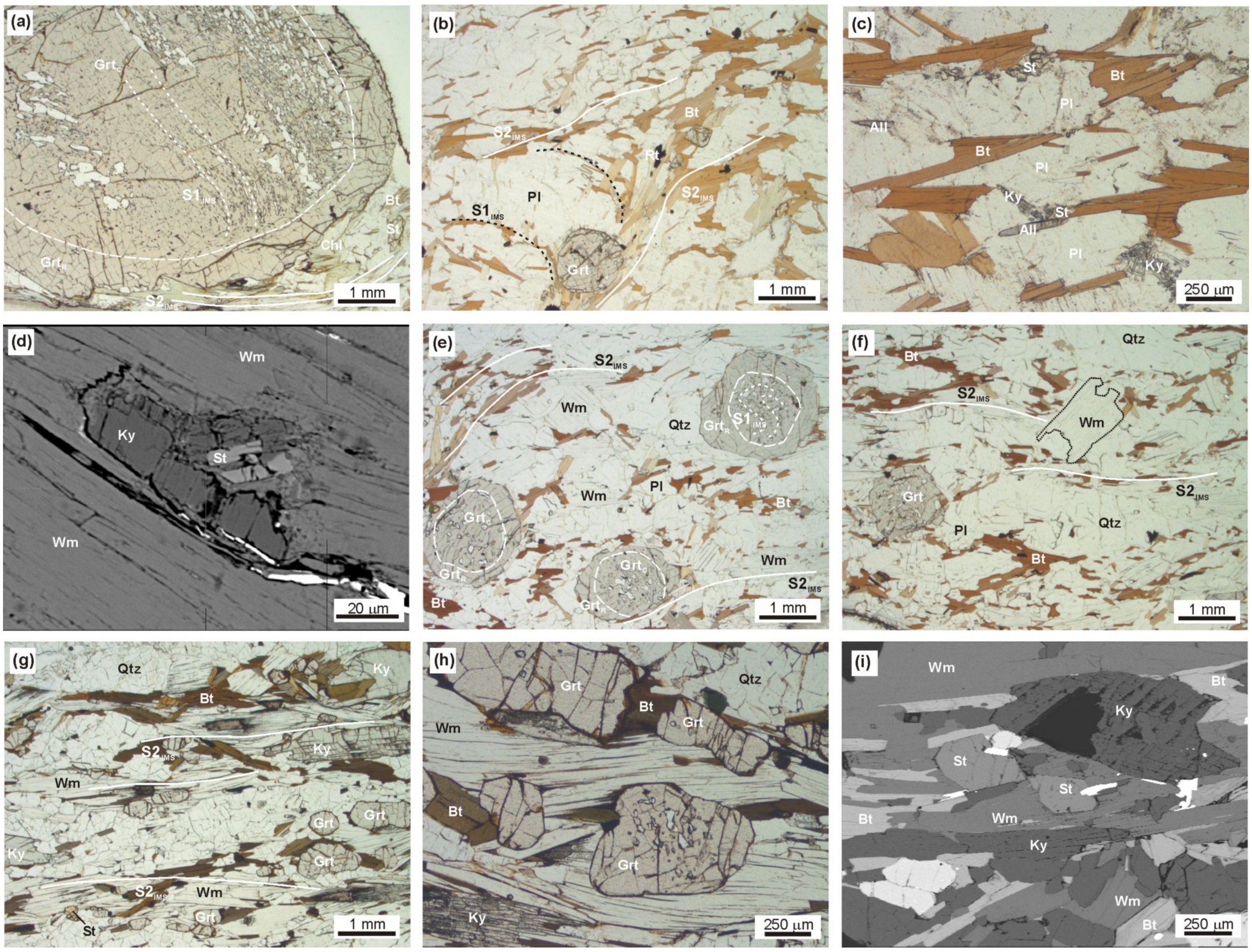

Sample 09-8b. (a) Garnet porphyroblast from a metapelitic level. Garnet core (GrtC) includes an internal foliation ($S1_{IMS}$) defined by quartz and ilmenite, whereas garnet rim (GrtR) is almost free of inclusions and in equilibrium with the main foliation $S2_{IMS}$ defined by chlorite, muscovite and biotite. Note the staurolite crystal on the right side of the microphoto (PPL). (b) Microstructure of a metapsammitic level: the main foliation, defined by biotite, is overgrown by garnet and plagioclase and derives from the transposition of an older $S1_{IMS}$ foliation. Rutile is present both within and outside garnet (PPL). (c) Detail of a metapsammitic level, showing plagioclase overgrowing the $S2_{IMS}$. Very fine-grained staurolite and kyanite grow at the interface between adjacent crystals of plagioclase (PPL) (d) Detail from a metapelitic level, showing fine-grained kyanite and staurolite crystals overgrowing the main $S2_{IMS}$ foliation defined by muscovite (BSE). Sample 09-9. (e) Garnet porphyroblasts showing a core (GrtC) crowded of quartz inclusions locally defining an internal foliation ($S1_{IMS}$), and a rim (GrtR) free of inclusions and in equilibrium with the main foliation ($S2_{IMS}$). The $S2_{IMS}$ is defined by muscovite and biotite (PPL). (f) Large muscovite flake overgrowing the $S2_{IMS}$. Note the plagioclase crystal in the same microstructural position, on the right side of garnet (PPL). Sample 09-12. (g) The main foliation $S2_{IMS}$ is defined by the alignment of muscovite, biotite, kyanite and staurolite (PPL). (h) Detail showing garnet rim partially overgrowing the $S2_{IMS}$ (PPL). (i) Detail showing kyanite both aligned with the $S2_{IMS}$ and overgrowing it (PPL).

The metapsammitic level consists of quartz, plagioclase, biotite, garnet, minor muscovite, very minor staurolite and kyanite, and accessory rutile and allanite. The main foliation, parallel to the $S2_{IMS}$ in the adjacent metapelitic level, is defined by the preferred orientation of biotite and muscovite (Bt >> Wm) and is overgrown by garnet and plagioclase porphyroblasts and by a later generation of biotite (Fig. 8b, c). Garnet porphyroblasts include both granoblastic and acicular rutile. Staurolite and kyanite locally occurs at the grain boundaries between adjacent plagioclase porphyroblasts (Fig. 8c), forming very small grains associated with quartz.

Mineral chemistry

Muscovite is the dominant phyllosilicate in the metapelitic level: its Si content ranges between 3.07 and 3.11 a.p.f.u., and Na is in the range 0.15-0.18 a.p.f.u. (Fig.

10c). No significant variations in composition have been observed for the white mica in the metapsammitic level. Biotite prevails in the metapsammitic level and occurs in two different generations (Fig. 10a): biotite in the $S2_{IMS}$ foliation has Ti=0.09-0.12 a.p.f.u. and X_{Mg}=0.49-0.52, whereas biotite statically overgrowing the $S2_{IMS}$ has a slightly higher X_{Mg} (Ti=0.10-0.11 a.p.f.u.; X_{Mg}=0.52-0.53). On average, biotite from the metapelitic level ($S2_{IMS}$) shows a lower X_{Mg} (Ti=0.09-0.13 a.p.f.u.; X_{Mg}=0.47-0.51). Chlorite (ripidolite) only occurs in the metapelite level (Si=5.21-5.24 a.p.f.u.; X_{Fe}=0.47-0.51).

Garnet porphyroblasts in both levels are strongly zoned but they are significantly different in composition (Fig. 10b). In garnet from the metapelitic level, the X_{Mn} and X_{Ca} decrease from core to rim (X_{Mn}= 0.07 to 0.00; X_{Ca}= 0.06 to 0.03), whereas X_{Mg} increases, initially slightly and then abruptly passing from 0.07 in the core to 0.18 in the rim. X_{Fe} increases from 0.79 in the core to 0.84 in the inner rim, and then decreases down to 0.78 in the outermost rim. Garnet from the metapsammitic level shows a decrease in X_{Mn} and X_{Ca} from core to rim (X_{Mn}=0.05 to 0.01; X_{Ca}=0.25 to 0.15) counterbalanced by an increase in both X_{Mg} and X_{Fe} (X_{Mg}=0.11 to 0.16; X_{Fe}=0.60 to 0.72).

Plagioclase is present only in the metapsammitic level. It is mostly an andesine (An31-37), with rare oligoclase cores (An_{18-21}) (Fig. 10d). Staurolite mostly occurs in the metapelitic level: its X_{Mg} varies from X_{Mg}=0.15-0.18 for the staurolite in equilibrium with the $S2_{IMS}$ foliation to X_{Mg}=0.14-0.16 for the staurolite overgrowing the $S2_{IMS}$. The fine-grained staurolite in the metapsammitic level has X_{Mg}=0.14-0.16.

Sample 09-9

Microstructure

Sample 09-9 is a coarse-grained two-micas, garnet-bearing micaschist. The main foliation ($S2_{IMS}$) is defined by the preferred orientation of muscovite and biotite (Wm ≈ Bt) occurring in mm thick micaceous levels alternated to quarzo-feldspathic domains (i.e. Qtz + Pl) (Fig. 8e, f). Large garnet porphyroblasts (up to several mm in diameter) are partially enveloped by the main foliation. More in detail, garnet porphyroblasts are microstructurally zoned: garnet core is crowded of inclusions (quartz, rutile and very fine-grained graphite) locally defining a rotated internal foliation ($S1_{IMS}$), whereas garnet rim is almost free of inclusions (Fig. 8e). Garnet rim is often discontinuous and appears in equilibrium with the $S2_{IMS}$ foliation. Large muscovite flakes and less frequent biotite lamellae statically overgrow the main foliation (Fig. 8f). Rutile is rimmed by ilmenite in the matrix.

Mineral chemistry

Except for the zoned garnet porphyroblasts, mineral compositions are extremely homogeneous thus reflecting the attainment of equilibrium. Biotite shows a Ti content in the range 0.18-0.21 a.p.f.u. and X_{Mg}=0.36-0.38 (Fig. 10a). White mica has Si=3.09-3.17 a.p.f.u. and low Na content (Na=0.07-0.09 a.p.f.u.) (Fig. 10c): no significant differences have been observed between muscovite in the $S2_{IMS}$ and muscovite post-$S2_{IMS}$. Plagioclase is oligoclase, with An=20-25 (Fig. 10d). Garnet is zoned, with X_{Mn} and X_{Ca} decreasing (X_{Mn}=0.07 to 0.02; X_{Ca}=0.13 to 0.11) and X_{Mg} and X_{Fe} increasing (X_{Mg}=0.07-0.11; X_{Fe}=0.72-0.75) from core to rim (Fig. 10b).

Sample 09-11

Microstructure

Sample 09-11 is a garnet-bearing, two-micas gneiss with a main foliation (S_m) defined by discontinuous micaceous levels (Bt > Wm) alternated with dominant quarzo-feldspathic layers (Fig. 9a). In the quartzo-feldspathic domains most of quartz and plagioclase are coarse-grained, whereas K-feldspar occurs as interstitial crystals, often with cuspate shapes (i.e. “melt pseudomorphs” according to the definition of Holness and Clemens, 1999; Holness and Sawyer, 2008). In those domains where K-feldspar is abundant, muscovite is absent. Plagioclase often presents a spongy rim due to the presence of very fine-grained K-feldspar exsolutions.

Figure 9. Representative microstructures of the structurally upper IMS anatectic metapelitic samples and of lower HHC “Barun-type” gneiss

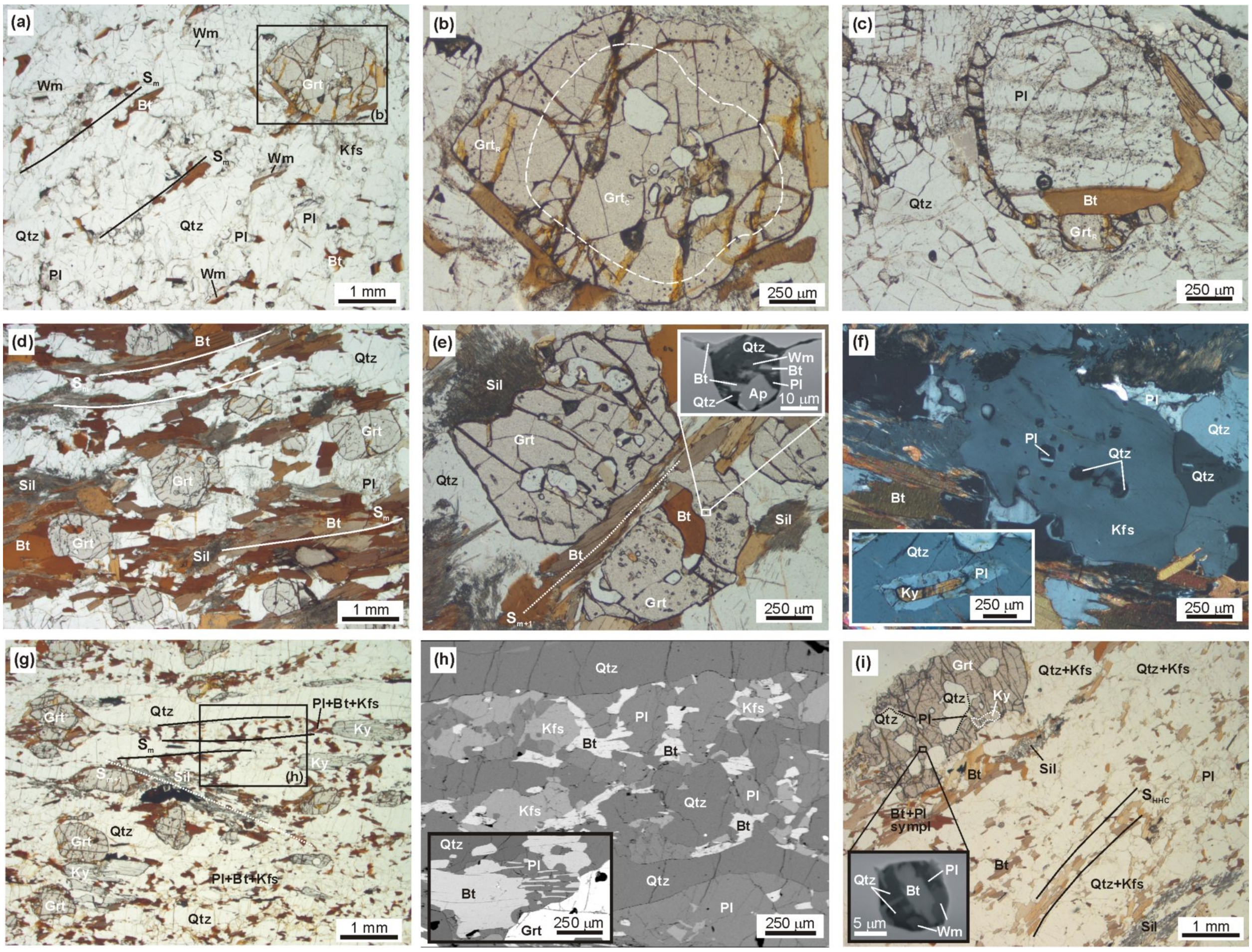

Sample 09-11. (a) The gneissic foliation S_m is defined by the alignment of both muscovite and biotite (PPL). (b) Detail of garnet porphyroblast shown in (a). Garnet core (GrtC) includes coarse grained rounded quartz, whereas garnet rim (GrtR) is crowded of very small polymineralic inclusions with a negative crystal shape (i.e. nanogranites) (PPL). (c) Detail of coronitic garnet isolating plagioclase and biotite from quartz. Note that coronitic garnet includes nanogranites as the garnet rim in (b) (PPL). Sample 09-13a. (d) The main foliation S_m is defined by the alignment of biotite, partially replaced by fibrolitic sillimanite, and overgrown by garnet porphyroblasts (PPL). (e) Detail of a garnet porphyroblast crosscut by a shear band defined by biotite + sillimanite (S_m+1). Garnet includes both coarse grained biotite and quartz and very small polymineralic inclusions (i.e. nanogranites) (PPL). One of these nanogranites, consisting of quartz, biotite, muscovite and albitic plagioclase is reported in the inset (BSE). (f) Detail of a coarse grained K-feldspar crystal with rounded inclusions of plagioclase and quartz, partially overgrowing the S_m (XPL). The inset shows a kyanite relict separated from quartz by a continuous corona of plagioclase (XPL). Sample 09-14. (g) The main foliation S_m is defined by the alternation of plagioclase + biotite + K-feldspar layers with elongated quartz rods. Garnet and kyanite are enveloped by the plagioclase + biotite + K-feldspar layers. The S_m is crosscut by later shear bands (S_m+1) defined by biotite + sillimanite (PPL). (h) Detail of the plagioclase + biotite + K-feldspar levels shown in (g) (BSE). The inset shows a detail of the biotite + plagioclase symplectitic microstructure developed at the interface between biotite and garnet (BSE). Sample 09-16a. (i) The gneissic foliation S_{HHC} is defined by biotite + sillimanite + plagioclase discontinuous mesocratic levels alternated with quartzo-feldspathic leucocratic layers (PPL). Garnet porphyroblast shows two types of inclusions: coarse-grained rounded quartz and kyanite surrounded by a thin film of plagioclase (“melt pseudomorph”) and “nanogranite” inclusions consisting of biotite, white mica, quartz and albitic plagioclase. One of these nanogranites is shown in the inset (BSE).

Garnet occurs in two different microstructural positions: (i) as mm large porphyroblasts set in the quartzo-feldspatic domains (Fig. 9b); (ii) as thin and discontinuous corona around plagioclase and/or biotite (Fig. 9c). The core of garnet porphyroblasts includes large and rounded inclusions of quartz, whereas the outermost rim is crowded of very small (tens of microns) birefringent inclusions which are too small to be deciphered at the optical microscope (Fig. 9b). At the SEM, these inclusions show a negative crystal shape and are polymineralic, generally consisting of quartz + muscovite ± biotite ± chlorite ± rutile. The same micrometric polymineralic inclusions are present in the garnet coronas developed at the interface between plagioclase and quartz or biotite and quartz. These inclusions are interpreted as "nanogranites" according to the definition of Cesare *et al.* (2009) and demonstrate that the rim of porphyroblastic garnet and coronitic garnet grew in the presence of melt, i.e. they are peritectic phases likely grown during de-hydration melting of muscovite (Vielzeuf and Holloway, 1988, Tajcmanova *et al.*, 2011).

Mineral chemistry

Biotite and muscovite have very homogeneous compositions (Fig. 10a, c): Ti content in biotite is in the range 0.16-0.21 a.p.f.u. and its X_{Mg} is 0.29-0.30, whereas the Si content in muscovite is 3.11-3.12 a.p.f.u. The microstructural zoning of plagioclase corresponds also to a chemical zoning: both plagioclase core and rim are oligoclase in composition (Fig. 10d), but the anorthite content of the core is lower than that of the rim (core: An_{11-17}, Or_{2-3}; rim: An_{15-20}, Or_{0-2}).

Figure 10. Compositional diagrams for biotite (a), garnet (b), white mica (c) and plagioclase (d) in the studied samples

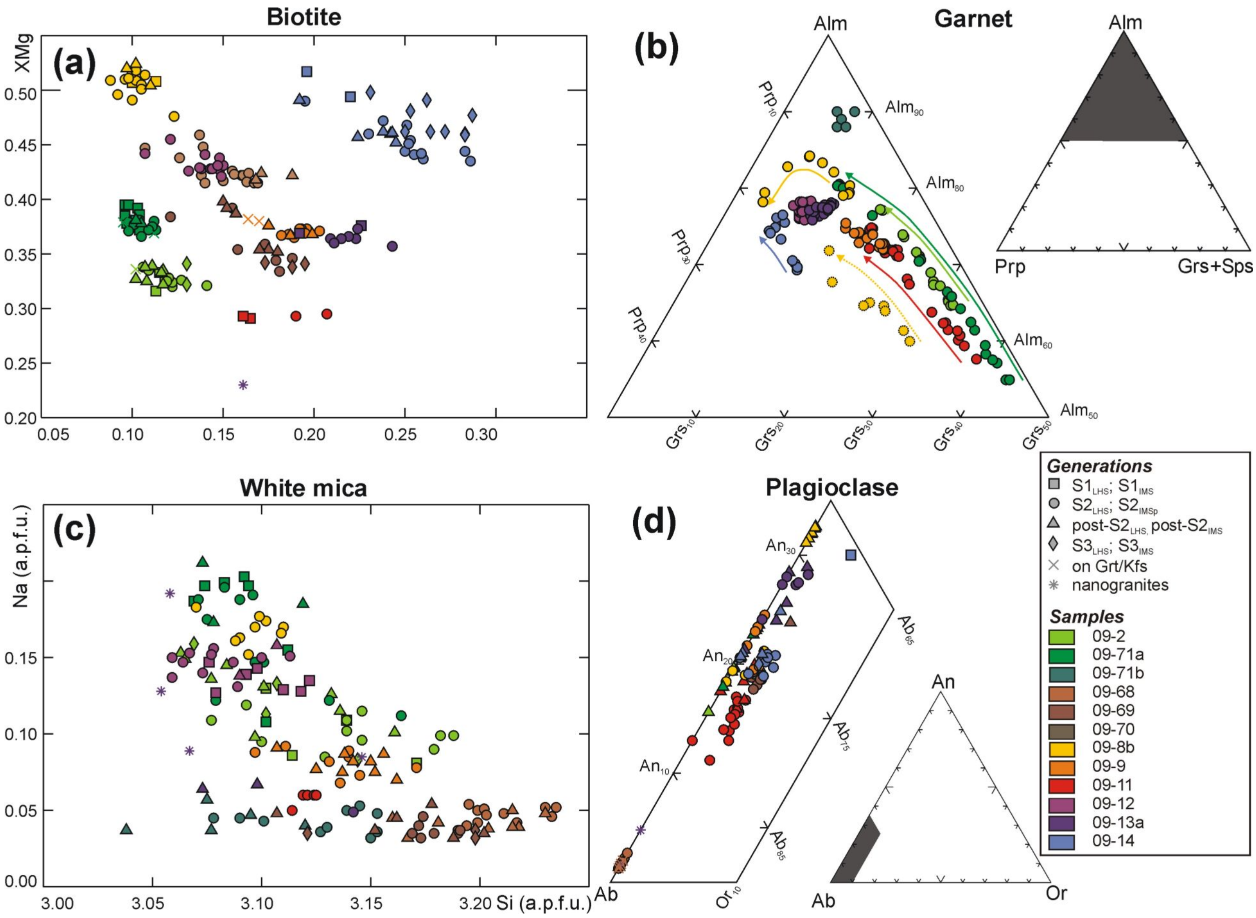

For each sample, biotite, muscovite and plagioclase have been distinguished according to their microstructural position. Garnet zoning from core to rim is indicated in (b) with coloured arrows; dotted vs. continuous arrows for sample 09-8b refer to garnet from meta-psammitic vs. metapelitic levels, respectively.

Garnet porphyroblasts are strongly zoned (Fig. 10b). Garnet cores show a bell-shaped decrease of X_{Mn} from 0.15 in the inner core to 0.03 in the outer core, counterbalanced by an increase in both X_{Mg} and X_{Fe} (X_{Mg}=0.04 to 0.09; X_{Fe}=0.58 to 0.72). The X_{Ca} trend is more complex, increasing from 0.22 to 0.24 and then decreasing down to 0.15. In the garnet rims crowded of "nanogranites", X_{Mn} and X_{Fe} increase (X_{Mn}=0.04 to 0.15; X_{Fe}=0.68

to 0.75) and X_{Mg} and X_{Ca} decrease (X_{Mg}=0.09 to 0.07; X_{Ca}=0.12 to 0.07). Coronitic garnet around plagioclase and/or biotite shows the same composition as the rim of porphyroblastic garnet, with the highest X_{Mn} and lowest X_{Mg} values toward the rim.

Sample 09-12

Microstructure

Sample 09-12 is a coarse-grained two-micas + garnet + staurolite + kyanite schist. The main foliation ($S2_{IMS}$) is defined by the preferred orientation of muscovite and biotite (Wm > Bt), which are concentrated in mm thick continuous layers alternated to quartz-rich domains (Fig. 8g). Locally, large muscovite flakes resembling mica-fish suggest that the main foliation $S2_{IMS}$ derived from the transposition of an older $S1_{IMS}$ foliation. Garnet occurs as mm large crystals which appear in equilibrium with the main foliation (Fig. 8g), except for the outermost rim that locally overgrows the $S2_{IMS}$ (Fig. 8h). Small quartz inclusions are locally present within garnet. Staurolite and kyanite occur as coarse-grained crystals either aligned with the $S2_{IMS}$ or overgrowing it (Fig. 8i). Neither staurolite nor kyanite are included in garnet; if in contact with garnet, they appear in equilibrium with it. Large muscovite flakes statically overgrow the main foliation.

Mineral chemistry

White mica occurs in three different generations (Fig. 10c): the large muscovite flakes enveloped by the main foliation (i.e. $S1_{IMS}$) show a Si content in the range 3.08-3.13 a.p.f.u. and Na=0.12-0.15 a.p.f.u.; muscovite defining the $S2_{IMS}$ shows a lower Si (Si=3.06-3.11 a.p.f.u.) counterbalanced by a slightly higher Na content (Na=0.14-0.16 a.p.f.u.); finally, the large muscovite flakes overgrowing the $S2_{IMS}$ have Si=3.09-3.11 a.p.f.u. and Na=0.14-0.16 a.p.f.u.. Biotite is quite homogeneous in composition (Fig. 10a) with Ti=0.11-0.15 a.p.f.u. and X_{Mg}=0.42-0.45.

Garnets are almost homogeneous (Fig. 10b), with X_{Mg}=0.15, X_{Ca}=0.04, X_{Mn}=0.05 and X_{Fe}=0.76: a slight decrease in X_{Mg} (down to 0.13), counterbalanced by an increase in X_{Mn}, is observed at the outermost rim. Staurolite is also homogeneous, with X_{Mg} ranging from 0.14 to 0.16.

Sample 09-13a

Microstructure

Sample 09-13a is a anatectic garnet + biotite + sillimanite gneissic micaschist, consisting of quartz, K-feldspar, plagioclase, biotite, sillimanite, and minor kyanite and muscovite. The main foliation (S_m) is defined by layers of biotite + sillimanite alternated with quartzo-feldspathic domains (Fig. 9d). Two types of quartzo-feldspathic domains may be recognised: (i) coarse-grained discontinuous levels mainly consisting of quartz (including very rare muscovite flakes) partially overgrown by fibrolitic sillimanite, and (ii) finer-grained K-feldspar + quartz + plagioclase layers. K-feldspar generally includes rounded quartz and/or plagioclase grains (i.e. peritectic K-feldspar: Fig. 9f) and it is partially corroded at its rim by plagioclase. Biotite occurs in two different microstructural positions: (i) it defines the S_m, where it appears partially replaced by fibrolitic sillimanite and overgrown by plagioclase granoblasts (Fig. 9d), and (ii) it defines mm thick shear bands (Fig. 9e), intersecting the S_m at low angles, in equilibrium with fibrolitic sillimanite.

Mm large crystals of garnet overgrow the main foliation S_m. Garnet is crowded of two different types of inclusions (Fig. 9e): (i) large mono- and/or polymineralic inclusions mainly consisting of rounded crystals of quartz and biotite; (ii) very small (tens of microns) polymineralic inclusions with negative crystal shape, consisting of quartz, biotite, white mica and albitic plagioclase in different proportions and generally including rutile or apatite crystals (i.e. “nanogranites” according to the definition of Cesare *et al.*, 2009) (Fig. 9e). These inclusions suggest that garnet is a peritectic phase grown during dehydration melting of biotite. Garnet crystals are locally crosscut by the biotite + sillimanite shear bands and they are partially corroded at their rim by fibrolitic sillimanite (Fig. 9e). Rare relict kyanite crystals, always rimmed by a plagioclase corona, also occur in the quartzo-feldspatic domains (Fig. 9f). Finally, rare muscovite flakes locally overgrow the main foliation.

Mineral chemistry

Biotite composition is quite homogeneous (Fig. 10a), independently from its microstructural position: Ti content is in the range 0.19-0.24 a.p.f.u. and X_{Mg}=0.36-0.38. Biotite in the very small polymineralic inclusions within garnet has a significant lower Ti and X_{Mg} contents (Ti=0.16 a.p.f.u.; X_{Mg}=0.23). Plagioclase is mainly an oligoclase (An21-29): on average, the lowest anorthite contents (An21-26) are observed in plagioclase overgrowing the S_m biotite (Fig. 10d). Plagioclase in the very "nanogranite" inclusions within garnet is albite (An2-5).

Garnet is almost unzoned (Fig. 10b), with X_{Mg}=0.13-0.14, X_{Ca}=0.04-0.05, X_{Mn}=0.05-0.06 and X_{Fe}=0.86-0.87; X_{Mg} slightly decreases toward the rim, down to X_{Mg}=0.11, counterbalanced by an increase in X_{Fe}. The rare muscovite flakes included in coarse-grained quartz have Si=3.14 a.p.f.u. and Na=0.05 a.p.f.u., whereas the late muscovite flakes statically overgrowing the S_m show lower Si (Si=3.07-3.10 a.p.f.u.) and higher Na (Na=0.06-0.07 a.p.f.u.) contents.

Sample 09-14

Microstructure

Sample 09-14 is a anatectic garnet + biotite + kyanite banded gneiss. The main foliation (S_m) is defined by mm thick continuous mesocratic layers consisting of biotite + plagioclase + K-feldspar alternated with leucocratic quartz domains, in which quartz mainly occurs as coarse-grained rods (Fig. 9g, h). Biotite in the mesocratic layers does not show any preferred orientation. Mm large garnet and kyanite crystals are partially enveloped by the mesocratic layers (Fig. 19g, h). Garnet mainly includes rounded quartz and rutile, especially in the core, and more rare biotite and plagioclase and is partially corroded by kyanite and biotite at its rim. Peculiar symplectitic microstructures consisting of biotite + plagioclase often occur at the contact between garnet and biotite (Fig. 9h). These symplectitic microstructures are generally interpreted, in anatectic rocks, as related to the late interactions between solids and melt (i.e. back-reactions), during final melt crystallization (e.g. Waters, 2001; Cenki *et al.*, 2002; Kriegsman and Álvarez-Valero, 2010). Mm thick and cm spaced shear bands, defined by biotite, sillimanite and plagioclase, crosscut the S_m at low angles (Fig. 9g).

Mineral chemistry

Biotite shows significant different compositions as a function of its microstructural position (Fig. 10a). Ti content is inversely proportional to X_{Mg}, varying in the range: Ti=0.20-0.23 a.p.f.u. (X_{Mg}=0.49-0.52) for biotite included in garnet, Ti=0.24-0.30 a.p.f.u. (X_{Mg}=0.43-0.47) for biotite in the mesocratic domains, Ti=0.20-0.26 a.p.f.u. (X_{Mg}=0.45-0.49) for biotite in the Bt + Pl symplectites and Ti=0.24-0.30 a.p.f.u. (X_{Mg}=0.46-0.50) for biotite in the shear bands. Plagioclase is oligoclase in composition (An19-25) and no significant compositional variations have been observed in different microstructural sites (Fig. 10d). Garnet is almost unzoned (Fig. 10b), with homogeneous X_{Mg}=0.19 and X_{Mn}=0.02, and a very slight decrease of X_{Ca} from 0.10 in the core to 0.05 in the rim, counterbalanced by a slight increase in X_{Fe} (X_{Fe}=0.80-0.83).

Higher Himalayan Cristallines

Sample 09-16a

Microstructure

Sample 09-16a is a biotite + garnet + K-feldspar + sillimanite + kyanite gneiss. The main foliation (S_{HHC}) is defined by thin discontinuous and mesocratic layers consisting of biotite, sillimanite ± fine-grained plagioclase alternated with centimetric leucocratic quartzo-feldspathic levels consisting of quartz and K-feldspar and minor coarse-grained anti-perthitic plagioclase (Fig. 9i). In the leucocratic domains, cuspate shaped domains of quartz and plagioclase are locally abundant in contact with rounded quartz, plagioclase and especially biotite: these microstructures are interpreted as "melt pseudomorphs" (Holness and Clemens, 1999; Holness and Sawyer, 2008).

Large garnet porphyroblasts (up to 1 cm in diameter) are present in the leucocratic layers (Fig. 9i). Two different types of inclusions have been observed within garnet porphyroblasts: (i) coarse grained mono- or poly-mineralic inclusions, mainly consisting of rounded quartz and/or corroded biotite and kyanite locally surrounded by a thin film of plagioclase, with garnet showing crystal faces toward plagioclase; (ii) very small birefringent inclusions (up to 20 microns in diameter) with a negative-crystal shape, mainly consisting of quartz, biotite, K-feldspar and albitic plagioclase in different proportions (i.e. "nanogranites" according to Cesare *et al.*, 2009). The two types of inclusions clearly suggest that garnet is a peritectic phase, grown in the presence of melt during de-hydration melting of biotite, at the expenses of quartz, biotite and kyanite. Garnet porphyroblasts are partially replaced at their rim by biotite + plagioclase symplectitic microstructures, interpreted as the result of back-reactions between solid and melt during final crystallization of the melt (e.g. Kriegsman and Àlvarez-Valero, 2010). Kyanite is rare and mainly included in garnet, whereas sillimanite is only present in the mesocratic discontinuous biotite + plagioclase layers defining the S_{HHC}.

Mineral assemblage and microstructural features of sample 09-16 are perfectly comparable with those described by Groppo *et al.* (2012) for the lateral equivalents Barun Gneisses of the Everest-Makalu region. The mineral chemistry and P-T evolution of these anatectic metapelitic gneisses has been already presented and modelled by Groppo *et al.* (2012), therefore they will not be further discussed in this paper.

Relative thermobarometry

In order to compare the P-T results with those obtained along another transect about 50 km westward in the Milke Danda ridge (Groppo *et al.*, 2009), peak and prograde metamorphic conditions for the studied samples were calculated using the same approach, software and database used by Groppo *et al.*, 2009. P-T conditions were estimated using the "Average PT" module in the THERMOCALC v. 3.25 software - (Powell and Holland, 1994) and the Holland and Powell (1998 – revised in 2002) thermodynamic dataset. Activity-composition relationships were calculated using AX. The "Average PT" method estimates P-T conditions using an independent set of reactions representing all the equilibria between the end-members of the equilibrium assemblage. This method has a number of advantages compared with conventional thermobarometry, including its consistency with other mineral equilibria methods (such as P-T pseudosections: e.g. Groppo *et al.*, 2009; Imayama *et al.*, 2010), and the possibility of realistic assignments of uncertainties. In addition, this method is able to find a result only if the given mineral assemblage defines a sufficient number of reactions between end-members that themselves intersect in the P-T range under investigation (i.e. "Average PT" is particularly suitable for low-variant assemblages).

The "Average PT" mode was used for all the samples except for samples 09-71a, 09-71b (LHS) and 09-68, 09-69, 09-70 (IMS orthogneiss) which do not define enough reactions for Average PT to work. Samples 09-71a and 09-71b represent different levels from the same outcrop: therefore, the "average T" mode was used for sample 09-71b - whose equilibrium assemblage defines very well constrained temperature conditions - and then the "average P" mode was used for sample 09-71a in order to obtain pressure conditions at the equilibration temperature resulting from sample 09-71b. For the anatectic samples 09-11, 09-13a and 09-14 possible complications arise from the presence of melt in equilibrium with the peak mineral assemblage. The melt solution model cannot be considered in the Average PT calculation. According to Clemens and Watkins (2001), the H_2O-undersaturated character of granitoid magmas derived from de-hydration melting of micas at high metamorphic grades, suggests that pure aqueous fluid is not usually present, in excess, at these conditions. This implies that αH_2O is mostly < 1 during the de-hydration melting processes. Therefore, the presence of melt in the equilibrium assemblages of samples 09-11, 09-13a and 09-14 was simulated by considering that a free fluid phase is lacking and that $\alpha H_2O < 1$. A $\alpha H_2O = 0.7$ was used for the three samples. Although this approach certainly simplifies the complexity of the problem, the obtained P-T results discussed in the following are consistent with petrogenetic grids, therefore we are confident that the relative P-T variations between samples (if not their absolute values) are quite realistic.

P-T results and preliminary considerations on the P-T paths

The pressures and temperatures (with the correspondent uncertainties) estimated by Average PT are reported in Table 6 and plotted in the P-T diagram of Fig. 12a. The "Average PT" approach allows to constrain P-T conditions corresponding to the growth of specific mineral assemblages, thus resulting in single P-T points in a P-T diagram. For the LHS and IMS not-anatectic samples, most of the obtained P-T results refer to the equilibrium assemblages defining the main foliation (i.e. $S2_{LHS}$, $S2_{IMS}$); in some cases, however, P-T constraints for the pre- and/or post-S2 assemblages have been also obtained (Table 6 and Fig. 12a). As concerning the anatectic samples from the structurally higher portion of the IMS, the obtained P-T results refer to the peak-T conditions, corresponding to the muscovite and biotite de-hydration melting event; only for sample 09-11, which preserves the prograde mineral assemblage and compositions, the prograde P-T conditions have been determined. Various sources of uncertainty (analytical precision, thermodynamic data, activity-composition relationships; Powell, 1978, 1985; Powell and Holland 1985; Fraser *et al.*, 2000) contribute to relatively large uncertainties (Fig. 12a) in the final THERMOCALC estimates (e.g. 1σ uncertainties on P-T results for the studied metapelites are generally greater than ± 30°C and ± 1.5 kbar). However, what is worth of notice in this approach, are not the absolute P-T values, but the relative differences between P-T conditions estimated for each sample.

Figure 11. Crystallization-deformation relations of the studied samples, with mineral compositions and synthesis of the thermobarometric results

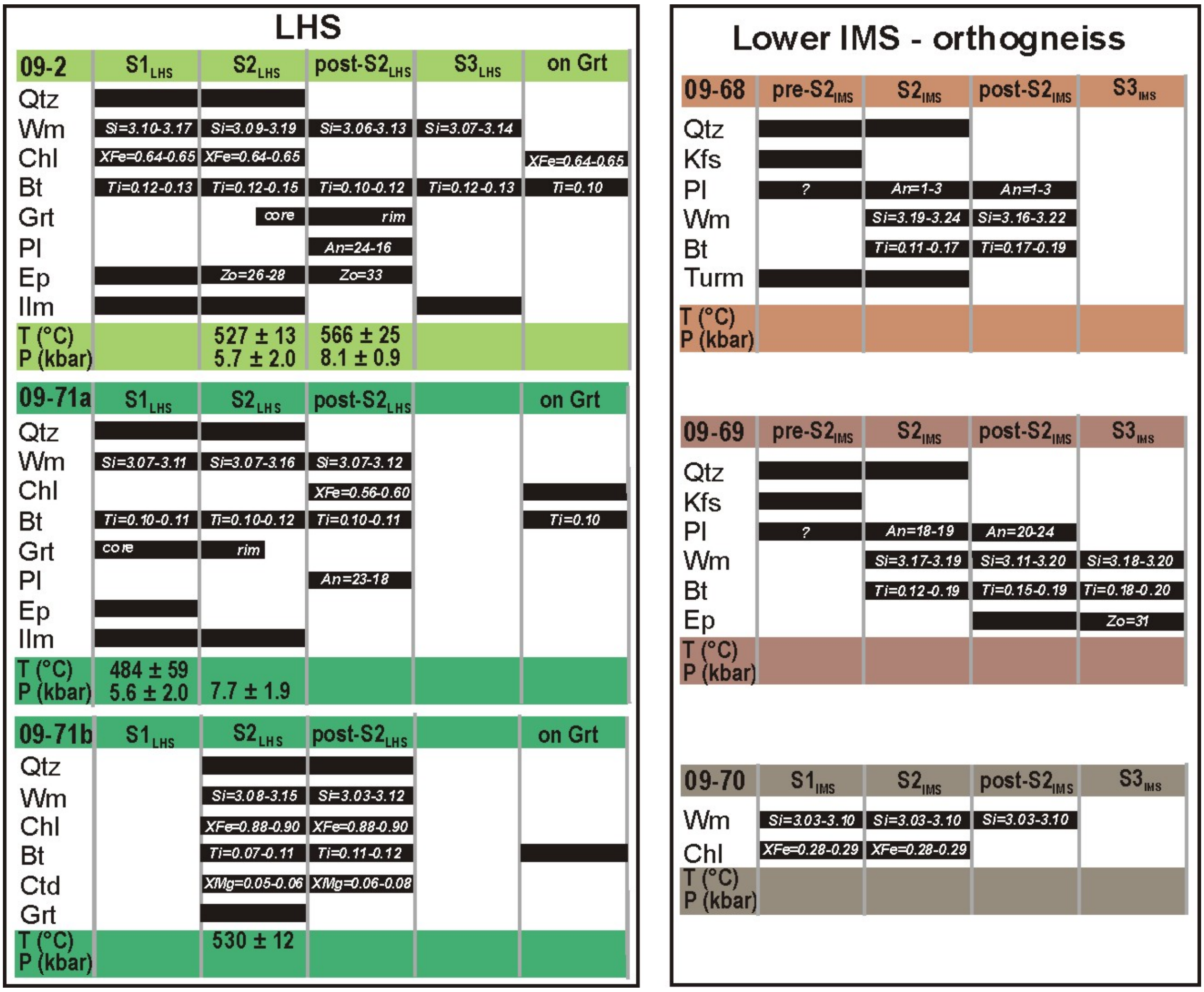

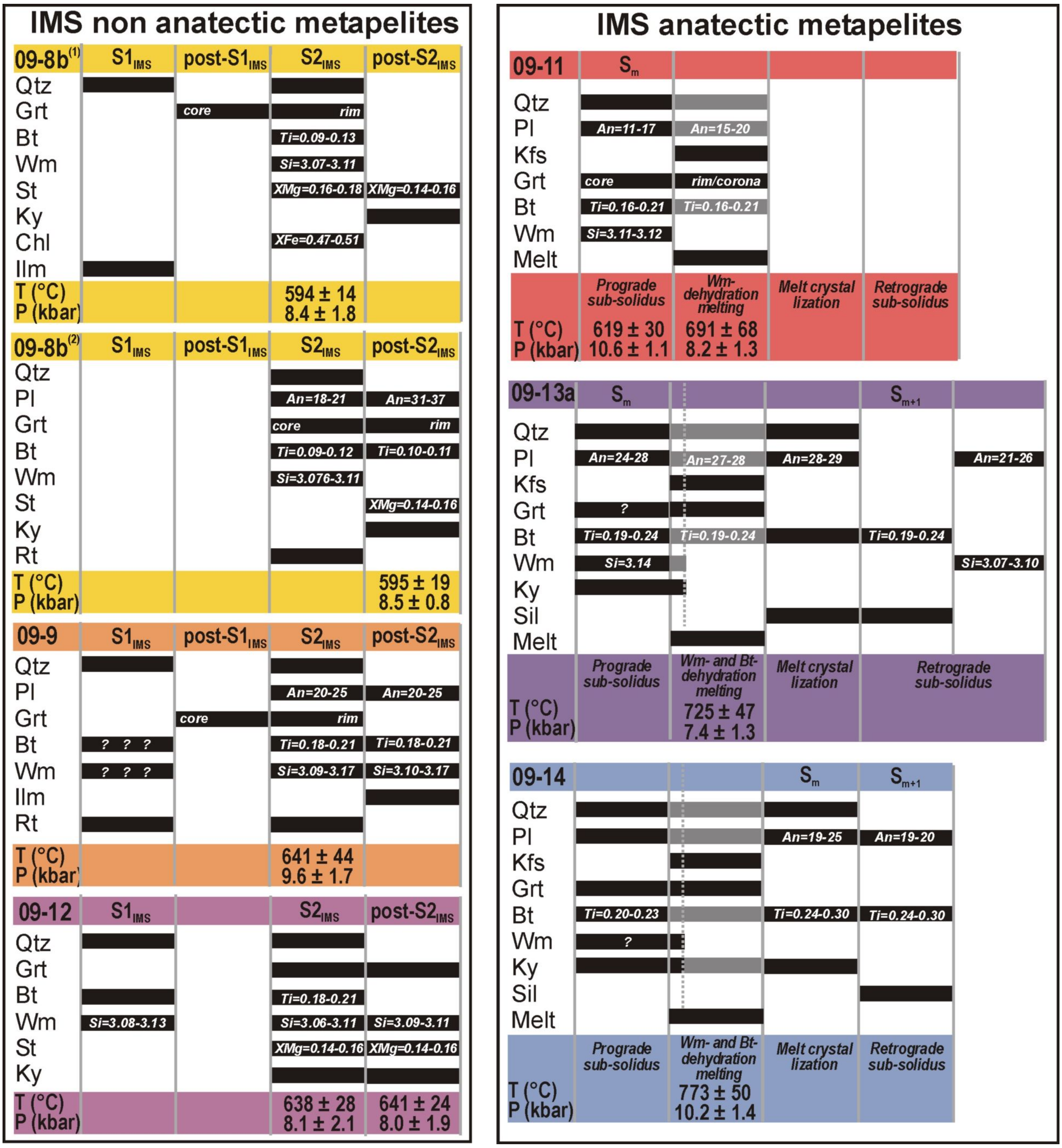

Colours for each sample are the same used in the next figures (a: LHS and lower IMS orthogneisses; b: lower and upper IMS metapelites). The following compositional parameters are shown: Si (a.p.f.u. on the basis of 22 oxygens) for white mica, Ti (a.p.f.u. on the basis of 22 oxygens) for biotite, X_{Fe} [X_{Fe}=Fe/(Fe+Mg)] for chlorite, An (x100) for plagioclase, X_{Mg} [X_{Mg}=Mg/(Fe+Mg)] for chloritoid and staurolite, Zo (x100) for epidote. For the upper IMS anatectic metapelites, the melting vs. crystallization relations are also shown (i.e. prograde sub-solidus crystallization, white mica ± biotite de-hydration melting, melt crystallization, retrograde sub-solidus crystallization): in the melt-bearing domain (muscovite ± biotite dehydration melting) grey vs. black bars discriminate between reactants and products of the melting reactions, respectively. In the anatectic samples, the development of oriented structures is not only controlled by deformational events, but also by the production, extraction and crystallization of the melt, therefore the correlation between the main foliation recognised in the lower IMS ($S2_{IMS}$) and that recognised in the upper IMS is not trivial. For this reason, the notation S_m (main schistosity) was preferred for the anatectic samples.

Figure 12. P-T diagrams showing the results of thermobarometry

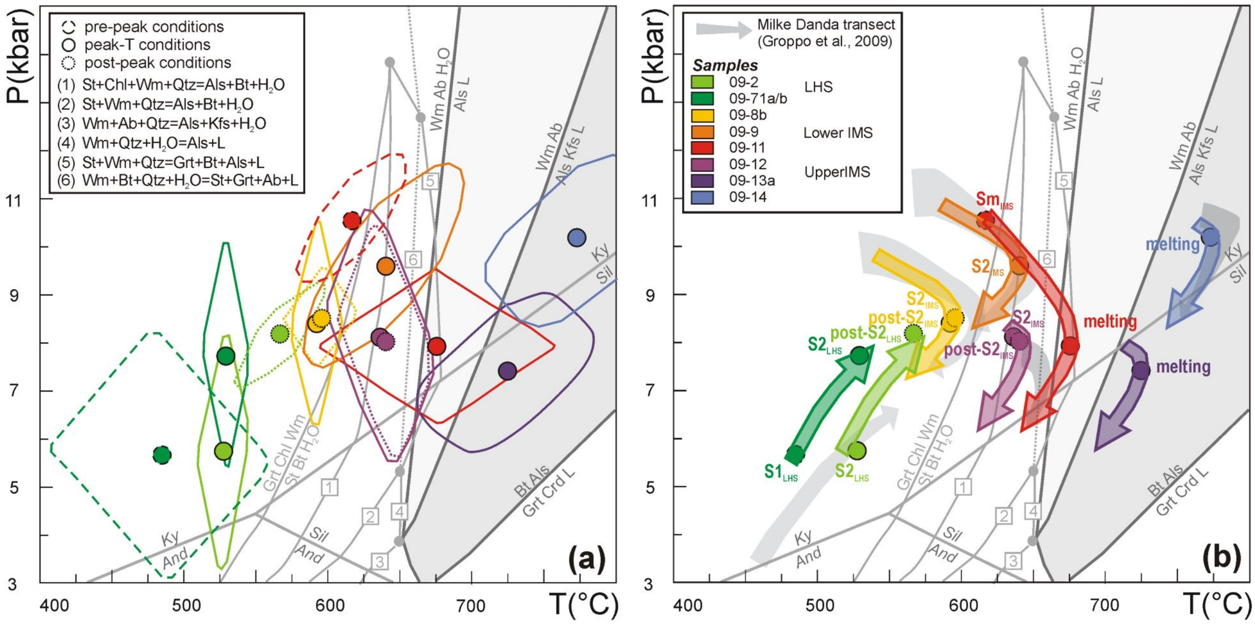

(a) P-T conditions estimated using the “Average PT” method applied to the low-variant equilibrium assemblages reported in Figure 6 and Table 6. 1σ error ellipses have been calculated using the parameters from THERMOCALC. NKFMASH petrogenetic grid (both thick and thin grey lines) are from Spear *et al.* (1999). The thick dark grey lines represent the main melt-producing reactions and delimitate the H_2O-saturated melting field (light grey field) from the H_2O under-saturated de-hydration melting of muscovite and biotite field (dark grey field). The thin light-grey lines constrain the stability field of staurolite according to Spear *et al.* (1999) and show a possible staurolite de-hydration melting reaction (reaction 5). (b) P-T paths inferred for the studied samples based on thermobarometric results and mineral compositions, and comparison with the P-T paths of the nearby Milke Danda transect (grey trajectories: Groppo *et al.*, 2009).

The main P-T results are summarized below, starting from the structurally lowermost samples.

i. The three phylladic micaschists from the LHS (samples 09-2, 09-71a and 09-71b) define similar peak P-T conditions of about 530-560°C, 7.7-9.1 kbar, corresponding to the development of the $S2_{LHS}$ and post-$S2_{LHS}$ assemblages. Sample 09-71a provides additional information about the LHS prograde evolution, suggesting an increase in both P and T from about 480-490°C, 5.0-5.5 kbar ($S1_{LHS}$ assemblage) up to peak metamorphic conditions (Fig. 12b).

ii. The mylonitic orthogneisses from the lowermost portion of the IMS do not define enough reactions for “Average PT” to work, therefore it is not possible to constrain P-T conditions of their equilibration in the framework of the same methods used for other samples.

iii. The results obtained from the lower IMS, not-anatectic, metapelitic samples 09-8b, 09-9 and 09-12 suggest that equilibration P-T conditions of the syn-$S2_{IMS}$ assemblages are approximately the same as those of the post-$S2_{IMS}$ assemblages (Fig. 12a), and in the range 600-650°C, 8.5-9.5 kbar (samples 09-8b and 09-9) and 640-650°C, ca. 8.0-8.1 kbar (sample 09-12). Samples 09-8b and 09-9 provide little information about their prograde evolution: garnet zoning (i.e. X_{Mg} increasing toward the rim) suggests an heating prograde evolution up to peak-T conditions coinciding with the syn-$S2_{IMS}$ assemblages (Fig. 12b), but does not provide information about pressure. On the contrary, garnet from sample 09-12 is almost unzoned, but muscovite composition (Si content is higher in the $S1_{IMS}$ muscovite with respect to the $S2_{IMS}$ muscovite) suggests that the $S1_{IMS}$ assemblage grew at higher pressure than the $S2_{IMS}$ assemblage (i.e. prograde decompression: Fig. 12b).

iv. As concerning the upper IMS anatectic metapelitic samples (09-11, 09-13a and 09-14), the “Average PT” results point to peak-T conditions in the range 680-770°C, 7.4-10.2 kbar. The lowest peak-T conditions (i.e. 680°C, sample 09-11) are compatible with the vapour-saturated melting of muscovite (Fig.

12b), producing very limited amounts of melt. This is consistent with microstructural observations, showing that muscovite is locally still preserved, but small amounts of peritectic garnet are also present. Peak-T conditions estimated for sample 09-13a and 09-14 (725-770°C) are consistent with H_2O-under-saturated de-hydration melting of muscovite (and eventually biotite) (Fig. 12b; Groppo *et al.*, 2012), as also evidenced by microstructures (i.e. absence of muscovite, presence of peritectic garnet and K-feldspar). The prograde history of such anatectic samples is difficult to be constrained mainly because mineral compositions were widely reset by diffusional re-homogenization at peak-T. Sample 09-11 preserves useful mineral compositional information, constraining a prograde heating and decompression evolution from about 620°C, 10.6 kbar to 680°C, 7.9 kbar (Fig. 12b). A heating and decompression evolution is also suggested (but not equally well constrained) for sample 09-14, basing on the garnet zoning (i.e. X_{Ca} decreasing toward the rim).

Discussions and conclusions

The structural architecture of the Himalayas in the investigated sector of far eastern Nepal is dominated at the regional-scale by the consistent dip to the north of tectonic boundaries and composite foliations, parallel to lithological contacts and compositional banding (Fig. 2). However, this apparently simple structural setting is the result of a high-strain and chronologically protracted deformational history, which was actually recorded in all the mapped tectonostratigraphic units by widespread transposition of earlier planar fabrics, and development of shear zones and mylonites.

As widely documented in other sectors of the Himalayan chain, also in the investigated sector of far eastern Nepal the southward extrusion and juxtaposition of the high-grade mid-crustal HHC over the low- to medium-grade metasedimentary LHS rocks is marked by the MCTZ, a north-dipping ductile to brittle-ductile shear zone showing minimum thickness on the order of 6-7 km in the north-western portion and 3-4 km in the south-eastern portion of the studied area (see profiles in Fig. 2; Mosca *et al.*, 2011). Considering the results of original field mapping and meso- and micro-structural data, the MCTZ has been here identified as a zone of “high strain” interesting both LHS and GHS and only roughly centred on the IMS, in which different lithologies are more pervasively deformed and sheared with respect to adjacent rocks. Neither a single thrust nor a set of adjacent, minor thrusts, have been identified and mapped in the field to clearly define the boundaries of the MCTZ. On the contrary, the lower ductile boundary of the MCTZ is marked by the occurrence of phyllonites and mylonitic schists in the uppermost portions of the LHS, immediately below the contact with strongly mylonitic augen-gneisses. The upper ductile boundary of the MCTZ is located at the base of the “Barun-type” gneiss (i.e. the lower portion of the HHC), and is characterized by evidence of pervasive ductile deformation and boudinage. Across the MCTZ and its adjacent domains the abundant kinematic indicators and pervasive stretching lineations mark an uniform top-to-south sense of regional thrusting.

Micro- and meso-structural data show that the distribution and the intensity of deformation is heterogeneous within the MCTZ, thus suggesting a partitioning of deformation into different deformation domains as usually observed within shear zones at different scales. This is also partly favoured by difference in lithological compositions, which results in contrasting rheology of the sheared rocks. Moreover, structural data combined with petrologic results clearly indicate that the MCTZ is internally imbricated, resulting in the juxtaposition of rock packages characterized by different P-T evolution and T/depth gradients. This is particular evident in Fig. 13, in which the peak P-T conditions recorded by the studied samples and the correspondent T/depth gradients are reported as a function of their structural level (i.e. present geometrical position). Fig. 13 shows that, although the peak-T appears to continuously increase from the lower to the upper structural levels of the MCTZ, three different rock packages – separated by “metamorphic discontinuities” – may be distinguished on the base of their T/depth gradients: (i) ~ 21°C/km for the LHS phyllites and schists; (ii) ~ 20°C/km for the lower IMS micaschists and gneisses, and (iii) ~ 25°C/km for the upper IMS micaschists and anatectic gneisses. These discontinuities revealed by thermobarometric results do not always correspond to structural discontinuities clearly evident on the field (i.e. single thrust or shear zones), being the whole MCTZ (as intended and presented above in this paper and in Mosca *et al.*, 2011) a zone highly strained: for this reason they are called “metamorphic discontinuities” (see also Groppo *et al.*, 2009 and Yakymchuk and Godin, 2012 for a similar use of this term). The lowermost metamorphic discontinuity (dashed line in Fig. 13) is approximately located at the lithological contact between the LHS phyllites and the IMS mylonitic augen gneisses, thus roughly coinciding with the MCT as originally defined by Heim and Gansser (1939) and Goscombe *et al.* (2006). On the contrary, the uppermost metamorphic discontinuity (dotted line in Fig. 13) is located within the IMS and does not coincide with any "conventionally" recognized major structure. The upper ductile boundary of the MCTZ, located structurally above the uppermost metamorphic discontinuity discussed in this paper (i.e. at the base of the "Barun-type" gneiss, possibly the equivalent of the HHT of Goscombe *et al.*, 2006), also represents an important metamorphic discontinuity.

Within the MCTZ, very similar results were obtained by Groppo *et al.* (2009) about 50 km westward, along the Milke Danda transect on the eastern side of the Arun tectonic window. In particular, peak P-T conditions estimated using the same method (i.e. "Average PT") are highly comparable between the two adjacent areas (Fig. 13), as well as are the qualitative P-T trajectories inferred for the studied samples on the base of mineral chemical data, garnet zoning and microstructural observations. This observation allows to speculate that the geometry of the P-T paths quantitatively very well constrained by Groppo *et al.* (2009) westward, could then be reasonably extended also eastward to the studied samples (Fig. 12b).

The results here obtained for the Kanchenjunga area confirm the existence of an important metamorphic discontinuity within the MCTZ (i.e. well above the MCT as originally defined by Heim and Gansser, 1939, but below the HHT of Goscombe *et al.*, 2006). This metamorphic discontinuity juxtaposes medium- to high-grade (locally anatectic) rocks that experienced moderate peak-P conditions, onto medium-grade rocks that experienced higher peak-P conditions. The existence of this discontinuity, firstly documented by Groppo *et al.* (2009) but already suggested by the P-T data presented by Goscombe *et al.* (2006) and Imayama *et al.* (2009) (Fig. 13), further supports the imbricated nature of the MCTZ (see also e.g. Yakymchuk and Godin, 2012) and suggests that the detailed comprehension of such a complex ductile shear zone can be only achieved by integrating structural, petrologic and geochronologic studies at different scales.

Acknowledgements

Field and laboratory work was carried out thanks to contributions from the CNR-IGG, UO Torino (P.M. and F.R.) and from PRIN Cofin 2006 and ex-60% founds (C.G. and F.R.). Further support by Ev-K2-CNR in the framework of SHARE - Stations at High Altitude for Research on the Environment - Project is also acknowledged. B. Lombardo is warmly thanked for lively discussions on Himalayan geology. Constructive comments and suggestions by S. Guillot and M. Zucali considerably improved the final version of the manuscript.

Figure 13. Temperatures (a) and pressures (b) referred to the peak metamorphic conditions, and T/depth ratios (c), reported as a function of structural level

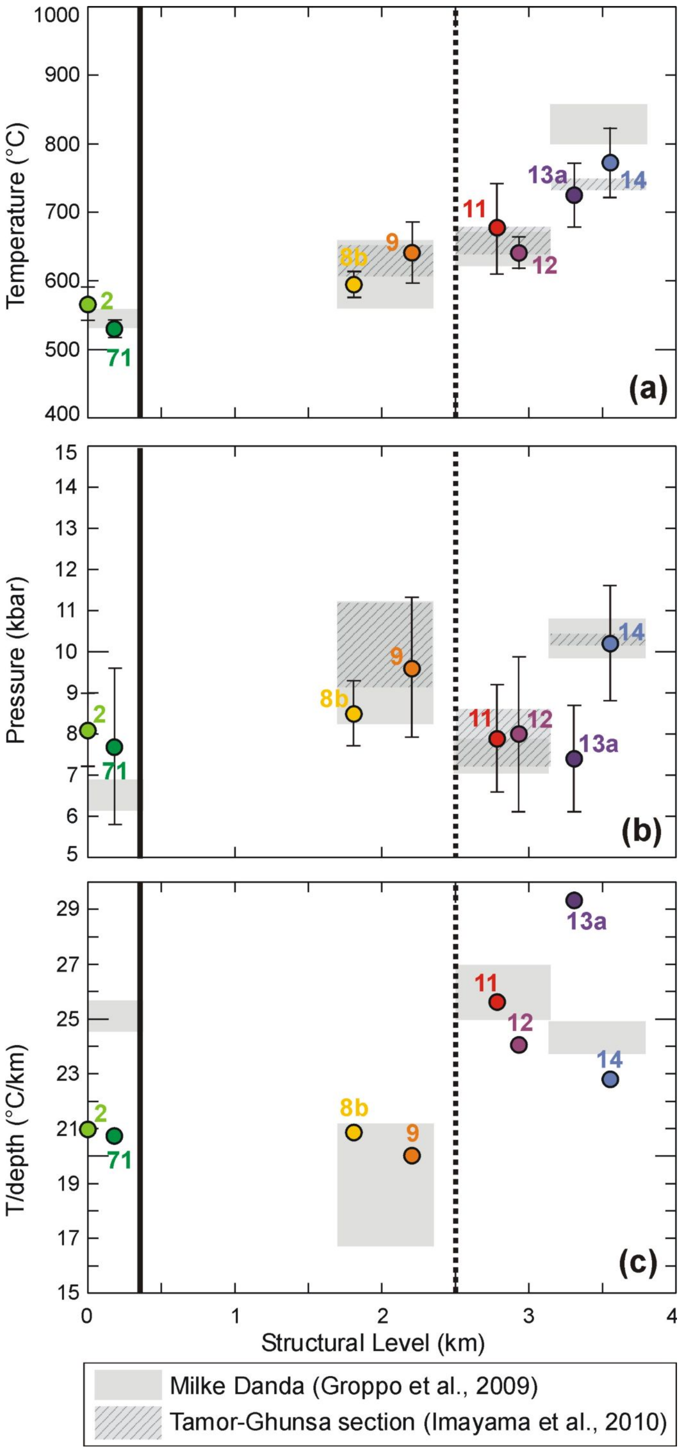

Structural level is calculated as the relative distance from the structurally lowest sample (09-2) and assuming an average lithostatic pressure gradient of 0.3 kbar/km. Error bars in the "Average P-T" data are 1σ errors. The dashed black line corresponds to the position of the MCT (as originally defined by Heim and Gansser, 1939), located at the base of the mylonitic augen-gneisses. The dotted black line represents the position of the inferred metamorphic discontinuity within the MCTZ, juxtaposing the upper IMS rocks characterized by higher T/depth gradients on the lower IMS rocks, characterized by lower T/depth gradients. Grey fields synthesize the main results of Groppo *et al.* (2009) and Imayama *et al.* (2010) along the Milke Danda and Tamor-Ghunsa Khola transects, respectively.

References

Arita, K., 1983. Origin of the inverted metamorphism of the Lower Himalayas, Central Nepal. Tectonophysics 93, 43-60.

Beaumont, C., Jamieson, R.A., Nguyen, M.H. and Lee, B., 2001. Himalayan tectonics explained by extrusion of a low-viscosity crustal channel coupled to focused surface denudation. Nature 414, 738–742.

Beaumont, C., Jamieson,R.A., Nguyen, M.H. and Medvedev, S., 2004.Crustal channel flows: 1. Numerical models with applications to the tectonics of the Himalayan–Tibetan orogen. Journal of Geophysical Research, 109 (B06406), 29 p., 10.1029/2003JB002809

Bordet, P., 1961. Recherches géologiques dans l'Himalaya du Népal, région du Makalu. Editions du Centre National de la Recherche Scientifique, Paris, 275 p.

Burchfield, B. C., Chen, Z.-L., Hodges, K. V., Liu, Y.-P., Royden, L. H., Deng, C.-R. & Xu, J.-N., 1992. The South Tibetan Detachment System, Himalayan Orogen. Geological Society of America Special Paper, 269, 1-41.

Carosi, R., Lombardo, B., Molli, G., Musumeci, G., and Pertusati, P.C., 1998. The South Tibetan Detachment System in the Rongbuk valley, Everest region. Deformation features and geological implications. Journal of Asian Earth Science 16, 299-311.

Cenki, B., Kriegsman, L.M. and Braun, I., 2002. Melt-producing and melt-consuming reactions in the Achankovil cordierite gneisses, South India. Journal of Metamorphic Geology 20, 543–561.

Cesare, B., Ferrero, S., Salvioli-Mariani, E., Pedron, D. and Cavallo, A., 2009. "Nanogranite" and glassy inclusions: the anatectic melt in migmatites and granulites. Geology 37, 627–630.

Clemens J.D. and Watkins, J.M., 2001. The fluid regime of high-temperature metamorphism during granitoid magma genesis. Contributions to Mineralogy and Petrology 140, 600-606.

Davidson, C., Grujic, D.E., Hollister, L.S. and Schmid, S.M., 1997. Metamorphic reactions related to decompression and synkinematic intrusion of leucogranite, High Himalayan Crystallines, Bhutan. Journal of Metamorphic Geology 15, 593–612.

DeCelles, P. G., Gehrels, G. E., Quade, J., Ojha, T.P., Kapp, P.A. and Upreti, B.N., 1998). Neogene foreland basin deposits, erosional unroofing, and the kinematic history of the Himalayan fold-thrust belt, western Nepal. Geological Society of America Bulletin., 110, 2-21.

Dietrich, V. and Gansser, A., 1981. The leucogranites of the Bhutan Himalaya (crustal anatexis versus mantle melting). Schweizerische Mineralogische und Petrographische Mitteilungen 61, 177-202.

England , P.C. and Molnar, P., 1993. The interpretation of inverted metamorphic isograds

using simple physical calculations. Tectonics 12, 145-157.

Fraser, G.,Worley, B. and Sandiford, M. 2000. High-precision geothermobarometry across the High Himalayan metamorphic sequence, Langtang Valley, Nepal. Journal of Metamorphic Geology 18, 665-681.

Gaetani, M. and Garzanti, E., 1991. Multiclycic history of the northern India continental margin (NW Himalaya). American Association of Petroleum Geologists Bulletin 75, 1427-1446.

Goscombe, B. and Hand, M., 2000. Contrasting P-T paths in the Eastern Himalaya, Nepal: inverted isograds in a paired metamorphic mountain belt. Journal of Petrology 41, 1673–1719.

Goscombe, B., Gray, D. and Hand, M., 2006. Crustal architecture of the Himalayan metamorphic front in eastern Nepal. Gondwana Research 10, 232–255.

Groppo, C., Rolfo, F. and Indares, A., (2012). Partial melting in the Higher Himalayan Crystallines of Eastern Nepal: the effect of decompression and implications for the "channel flow" model. Journal of Petrology 53, 1057-1088.

Groppo, C., Rolfo, F. and Lombardo, B., 2009. P-T evolution across the Main Central Thrust Zone (Eastern Nepal): hidden discontinuities revealed by petrology. Journal of Petrology 50, 1149–1180.

Groppo, C., Rubatto, D., Rolfo, F. and Lombardo, B. 2010. Early Oligocene partial melting in the Main Central Thrust Zone (Arun Valley, eastern Nepal Himalaya). Lithos 118, 287–301.

Grujic, D., Hollister, L.S. and Parrish, R.R., 2002. Himalayan metamorphic sequence as an orogenic channel: insight from Bhutan. Earth and Planetary Science Letters, 198, 177–191.

Guillot, S., 1999. An overview of the metamorphic evolution in Central Nepal. Journal of Asian Earth Sciences, 17, 713-725.

Guillot, S., Garzanti, E., Baratoux, D., Marquer, D., Mahéo, G. & de Sigoyer, J., 2003. Reconstructing the total shortening history of the NW Himalaya. Geochemistry Geophysics Geosystems, 4.

Guillot, S. and Le Fort, P., 1995. Geochemical constraints on the bimodal origin of High Himalayan leucogranites. Lithos, 35(3-4), 221-234.

Harrison, T. M., Grove, M., Lovera, O.M., Catlos, E.J. and D'Andrea, J., 1999, The origin of Himalayan anatexis and inverted metamorphism: Models and constraints. Journal of Asian Earth Sciences, 17 , 755-772.

Heim, A. and Gansser, A.,1939. Central Himalaya: geological observations of the Swiss expedition, 1936. Memoires de la Société Helvetique de Sciences Naturelles, 73, 1–245.

Hey, M. H., 1954. A new review of the chlorites. Mineralogical Magazine 30, 224, 277-292.

Hodges, K.V., 2000. Tectonics of the Himalaya and southern Tibet from two perspectives. Geological Society of America Bulletin, 112/3, 324-350.

Holland, T.J.B. and Powell, R., 1998. An internally consistent thermodynamic data set for phases of petrologic interest. Journal of Metamorphic Geology 16, 309–343.

Holness, M.B. and Clemens, J.D., 1999. Partial melting of the Appin Quartzite driven by fracture controlled H2O infiltration in the aureole of the Ballachulish Igneous Complex, Scottish Highlands. Contributions to Mineralogy and Petrology 136, 154–168.

Holness, M.B. and Sawyer, E.W., 2008. On the pseudomorphing of melt-filled pores during the crystallization of migmatites. Journal of Petrology 49, 1343–1363.

Imayama, T., Takeshita, T. and Arita, K., 2010. Metamorphic P–T profile and P–T path discontinuity across the far-eastern Nepal Himalaya: investigation of channel flow models. Journal of Metamorphic Geology 28, 527–549.

Kellet, D. A., Grujic, D, Warren, C., Cottle J., Jamieson, R. and Tenzin, T., 2010. Metamorphic history of a syn-convergent orogen-parallel detachment: The South Tibetan detachment system, Bhutan Himalaya. Journal of Metamorphic 28, 785-

Kohn, M.J., Paul, S.K. and Corrie, S.L., 2010. The lower Lesser Himalayan sequence: A Paleoproterozoic arc on the northern margin of the Indian plate, 2010, Geological Society of America Bulletin, 122, 3/4, 323–335.

Kriegsman, L.M. and Álvarez-Valero, A.M., 2010. Melt-producing versus melt-consuming reactions in pelitic xenoliths and migmatites. Lithos 116, 310–320.

Leech, M.L., Singh, S., Jain, A.K., Klemperer, S.L., Manickavasagam, R.M., 2005. The onset of India–Asia continental collision: early, steep subduction required by the timing of UHP metamorphism in thewestern Himalaya. Earth and Planetary Science Letters 234, 83–97.

Le Fort, P., 1975. Himalaya: the collided range. Present knowledge of the continental arc. American Journal of Science 275A, 1–44.

Le Fort, P., 1996. The Himalayan evolution. In: Yin, A., Harrison, T.M. (Eds.), The Tectonics of Asia. Cambridge University Press, New York, 95-109.

Lombardo, B., Pertusati, P. and Borghi, A., 1993. Geology and tectono-magmatic evolution of the eastern Himalaya along the Chomolungma-Makalu transect. In: Treloar, P.J. and Searle, M.P. (eds.) Himalayan Tectonics. Geological Society of London, Special Publication 74, pp. 341–355.

McQuarrie, N., Robinson, D., Long, S., Tobgay, T., Grujic, D., Gehrels, G., and Ducea, M., 2008. Preliminary stratigraphic and structural architecture of Bhutan: Implications for the along strike architecture of the Himalayan system. Earth and Planetary Science Letters 272, 105–117.

Mitra, G., Bhattacharyya, K and Mukul, M., 2010. The Lesser Himalayan Duplex in Sikkim: Implications for Variations in Himalayan Shortening. Journal Geological Society of India, 75, 289-301.

Mosca, P., Groppo., C., and Rolfo F., (2011) Geological and structural architecture of the Kangchenjunga region in Eastern Nepal. Journal of Nepal Geological Society, 43 (Special Issue), 1-12

Paudel, L.P. and Arita, K., 2000. Tectonic and polymetamorphic history of the Lesser Himalayan in central Nepal. Journal of Asian Earth Sciences, 18, 561-584.

Pêcher,A.,1989. The metamorphism in Central Himalaya. Journal of Metamorphic Geology 7, 31–41.

Pognante, U. and Benna, P., 1993. Metamorphic zonation, migmatization, and leucogranites along the Everest transect (Eastern Nepal and Tibet): record of an exhumation history. In: Treloar, P.J. and Searle, M.P. (eds.) Himalayan Tectonics. Geological Society of London, Special Publication 74, 323–340.

Pouchou, J.L. and Pichoir, F., 1988. Determination of mass absorption coefficients for soft X-Rays by use of the electron microprobe. Microbeam Analysis, San Francisco Press, 319–324.

Powell, R. and Holland, T. J. B., 1994. Optimal geothermometry and geobarometry. American Mineralogist 79, 120-133.

Powell, R. and Holland, T. J. B., 1985. An internally consistent dataset with uncertainties and orrelations: 1. Methods and a worked example. Journal of Metamorphic Geology 3, 327-342.

Powell, R., 1978. Equilibrium Thermodynamics in Petrology (an Introduction). London: Harper & Row, 295 pp.

Powell, R. 1985. Geothermometry and geobarometry: a discussion. Journal of the Geological Society of London 142, 29-38.

Rowley, D.B., 1996. Age of initiation of collision between India and Asia: a review of stratigraphic data. Earth and Planetary Sciences Letter 145, 1-13.

Schelling, D. and Arita, K., 1991. Thrust tectonics, crustal shortening, and the structure of the far-eastern Nepal Himalaya. Tectonics 10, 851-862.

Schelling, D., 1992. The tectonostratigraphy and structure of the eastern Nepal Himalaya. Tectonics 11 (5), 925-943.

Searle, M. P., Law, R. D., Godin, L., Larson, K. P., Streule, M. J., Cottle, J. M. and Jessup, M. J., 2008. Defining the Himalayan Main Central Thrust in Nepal. Journal of the Geological Society of London 165, 523–534.

Searle, M.P. and Rex, A.J.,1989. Thermal model for the Zanskar Himalaya. Journal of Metamorphic Geology 7, 127–134.

Shrestsa, S. B., Shrestsa, J. N. and Sharma, S. R., 1984. Geological Map of Eastern Nepal, 1:250.000. Ministry of Industry, Department of Mines and Geology, Lainchour, Kathmandu.

Solar, G.S., 2008. The interplay between tectonics/structure and migmatite morphology in the field. Mineralogical Association of Canada Short Course, 38, 145-158.

Spear, F.S., Kohn, M.J. and Cheney, J.T.,1999. P-T paths from anatectic pelites. Contributions to Mineralogy and Petrology 134, 17–32.

Stephenson, B. J., Waters, D. J. and Searle, M.P., 2000. Inverted metamorphism and the Main Central Thrust: field relations and thermobarometric constraints from the Kishtwar Window, NW Indian Himalaya. Journal of Metamorphic Geology 18, 571–590.

Tajcmanova L., Bartoli O., Cesare B. and Acosta-Vigil, A., 2011. Constraining the P-T conditions of melting in stromatic migmatites from Ronda (S Spain). Epitome Geoitalia 2011, 4, 169.

Upreti, B.N., 1999. An overview of the stratigraphy and tectonics of the Nepal Himalaya. Journal of Asian Earth Sciences 17, 577–606.

Vannay, J.-C. and Grasemann, B., 2001. Himalayan inverted metamorphism and syn-convergence extension as a consequence of a general shear extrusion. Geological Magazine, 138 , 253-276, 10.1017/S0016756801005313

Vielzeuf, D. and Holloway, J. R., 1988. Experimental determination of the fluid-absent melting relations in the pelitic system. Contributions to Mineralogy and Petrology 98, 257-276.

Visonà, D. and Lombardo, B., 2002. Two mica- and tormaline leucogranites from the Everest-Makalu region (Nepal-Tibet): Himalayan leucogranite genesis by isobaric heating? Lithos 62, 125–150.

Waters, D.J., 2001. The significance of prograde and retrograde quartz-bearing intergrowth microstructures in partially melted granulite-facies rocks. Lithos 56, 97–110.

Whitney, D. L. and Evans, B. W., 2010. Abbreviations for names of rock-forming minerals, American Mineralogist, 95, 185–187.

Yakymchuk, C. and Godin, L., 2012. Coupled role of deformation and metamorphism in the construction of inverted metamorphic sequences: an example from far-northwest Nepal. Journal of Metamorphic Geology 30, 513-535.